MASTER

DR. 266
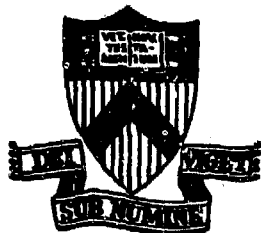
PARAMETRIC DECAY INTO ION CYCLOTRON WAVES AND DRIFT WAVES IN MULTI-ION-SPECIES PLASMA

BY

M. ONO, M. PORKOLAB, R. P. H. CHANG

PLASMA PHYSICS LABORATORY

PRINCETON   UNIVERSITY
PRINCETON, NEW JERSEY

PARAMETRIC DECAY INTO ION CYCLOTRON WAVES AND DRIFT WAVES IN MULTI-ION-SPECIES PLASMA

M. Ono

Plasma Physics Laboratory, Princeton University
Princeton, New Jersey   08544

and

M. Porkolab

Department of Physics and Plasma Fusion Center
Massachusetts Institute of Technology. Cambridge, MA   02139

and

R.P.H. Chang

Bell Laboratories, Murray Hill, New Jersey   07974

ABSTRACT

Parametric decay processes near the ion cyclotron frequency are investigated experimentally and theoretically in multi-ion species plasmas.   The relevant theoretical dispersion relation of the parametric coupling is derived, including the ion drift motion.   Experimental data obtained in the Princeton L-4 device verifies these theoretical predictions in some detail.   In a helium-neon plasma, the relative ion drift motion excites electrostatic ion cyclotron waves (the kinetic ion-ion hybrid mode) when $\omega_0 > \Omega_{He} + \Omega_{Ne}$. In a region of large density gradient, the ion drift motion also excites low frequency drift waves when $\omega_0 > \Omega_{He} + \omega^{\star}$. The experimental data are found to agree well with the theory. The relevance of these processes to ICRF heating of fusion plasmas is pointed out.

I. INTRODUCTION

In order to heat laboratory plasmas to fusion ignition temperatures, the application of radio frequency electric fields near the ion cyclotron frequency (ICRF) is currently under intensive experimental and theoretical investigations. In the past, high power ICRF heating experiments had successfully demonstrated efficient coupling of the RF power to plasmas via RF induction coils which yielded significant increase in the ion temperature.[1,2] However, near the ion cyclotron frequency a variety of modes, resonances and cutoffs may occur, and consequently the physics of wave phenomena can be rich and complex.

As the intensity of the applied RF electric field increases, parametric instabilities can become important since the threshold electric fields for their excitation are relatively low. By exciting short wavelength electrostatic decay waves which are quickly absorbed by the plasma, parametric instabilities can significantly change the heating processes. Theoretical investigations of parametric instabilities for the pump frequency in the vicinity of the ion cyclotron frequency (i.e. $\omega_0 = O(\Omega_i)$) have been carried out by many groups.[3-8] In a multi-ion-species plasma, for $\omega_0 = O(\Omega_i)$ the relative ion-ion drift motion can be significant and can excite parametric instabilities.[5-8] Preliminary results of experimental observations of some of these instabilities have been reported recently.[9,10,11]

In this paper we present a more detailed account of our work
regarding parametric excitation in the ion cyclotron regime.
The multi-ion-species effects can become important in the ICRF
heating of a D-T fusion plasma and also in the isotope separa-
tion scheme using ICRF heating.[12,13] The plan for this paper is
as follows:

In Sec. II, we derive the general dispersion relation
of parametric instabilities in multi-ion-species plasmas.
We shall then consider parametric excitation of electro-
static ion cyclotron waves and drift waves in a two-ion-
species plasma. The emphasis will be on the theory which
is relevant to our experiments. For decay into the low
frequency drift waves, the calculation requires an inclusion
of the upper sideband and frequency mismatch terms. Since
such a calculation can be tedius, the details are given in
Appendix A.

Section III is composed of three parts, labeled A,B,
and C, in which we describe our experimental set-up. In
part A, we describe the overall aspects of the experimental
device L-4 and the plasma source. In part B, we describe
techniques to measure the ion concentration ratios. In
part C, the RF set-up is described.

In Section IV, we present experimental data on two instabilities which are observed in our experiments. In part A, parametric excitation of the electrostatic ion cyclotron waves in a two-ion-species plasma is presented.[9,10] In part B, we present evidence of parametric excitation of the low frequency drift waves in two-ion-species plasmas.[11] These decays are driven by the relative ion-ion drift motion. Finally, in Section V, we present the summary and conclusions of the present work.

II. THE THEORY OF PARAMETRIC INSTABILITY

A. DERIVATION OF THE DISPERSION RELATION

In this section, we consider a general dispersion relation of parametric instability near the ion cyclotron frequency in a multi-ion-species plasma. The pump electric field is assumed to be uniform and is expressed in the following form:

$$\vec{E} = \vec{E}_0 \cos (\omega_0 t),$$

where ω_0 is the pump frequency and $\vec{E}_0$ is the pump electric field amplitude. The polarization of the electric field is implicitly included in $\vec{E}_0$. The selection rules for the parametric coupling equation can be expressed in the following form:

and
$$\omega_0 = \omega + |\omega^-| \tag{1a}$$

$$\vec{k}_0 = 0 = \vec{k} + \vec{k}^- \tag{1b}$$

where $(\omega, \vec{k})$ and $(\omega^- = \omega - \omega_0, \vec{k}^-)$ are the frequencies and the wave numbers of the low frequency and the lower sideband modes, respectively. Then a set of coupled equations for the charge, $\rho_\sigma(\omega, k)$, and the potential $\phi(\omega, k)$ can be obtained in the following form:[14,15]

$$\rho_\sigma(\omega, k) = - \frac{k^2}{4\pi} \sum_{n=-\infty}^{\infty} J_n(\mu_\sigma) \exp(-in\beta_\sigma) \chi_\sigma(\omega, k) \phi(\omega + n\omega_0, k), \tag{2a}$$

and $\qquad \phi(\omega,k) = \dfrac{4\pi}{k^2} \displaystyle\sum_\sigma \sum_{n=-\infty}^{\infty} J_n(-\mu_\sigma) \exp(-in\beta_\sigma)\rho_\sigma(\omega+n\omega_0,k)$, $\qquad$ (2b)

where σ designates the electron and all the ion species, $\mu_\sigma = \vec{V}_\sigma \cdot \vec{k}/\omega_0$ is the ratio of drift excursion to the wave length of the decay mode, β_σ is a phase angle, χ_σ is the plasma susceptability, k is the decay wave number, and J_n is the ordinary Bessel function of order n. For a plane-polorized pump wave, $E_0 = E_{0x}\hat{x} + E_{0y}\hat{y} + E_{0z}\hat{z}$, μ_σ can be expressed more explicitly as,

$$\mu_\sigma = \frac{q_\sigma}{m_\sigma}\left[\left(\frac{E_{0\parallel}k_z}{\omega_0^2} + \frac{E_{0\perp}\cdot k_\perp}{\omega_0^2-\Omega_\sigma^2}\right)^2 + \frac{(E_{0x}k_y-E_{0y}k_x)^2\Omega_\sigma^2}{(\omega_0^2-\Omega_\sigma^2)^2\omega_0^2}\right]^{1/2}$$

where the external magnetic field points in the $\hat{z}$ direction.

Using Eq. (2a) one can eliminate ρ_σ in Eq. (2b) and obtain the following set of coupled equations for the potential ϕ:

$$\phi(\omega)\ [1 + \sum_\sigma \sum_{n=-\infty}^{\infty} J_n(-\mu_\sigma)J_{-n}(\mu_\sigma)\chi_\sigma(\omega+n\omega_0)\ ]$$
$$= -\sum_\sigma \sum_{n=-\infty}^{\infty} \sum_{\substack{m=-\infty\\m\neq 0}}^{\infty} e^{-im\beta_\sigma}J_n(-\mu_\sigma)J_{m-n}(\mu_\sigma)\chi_\sigma(\omega+n\omega_0)\phi(\omega+m\omega_0),$$ $\qquad$ (3)

where the argument k was deleted since it is understood. In order to reduce Eq. (3) to simpler dispersion relation for parametric coupling, this infinite set of coupled equations has to be truncated at some point. Here we shall retain the plasma suscentabilities with frequencies, ω, $\omega-\omega_0$, and $\omega+\omega_0$. We have also carried out a calculation including the higher harmonic terms. However, their inclusion did not significantly alter the solution as long as

μ_σ was not large ($\mu_\sigma < 1$). For a notational simplicity, we shall define $f(\omega)$ as f, $f(\omega-\omega_0)$ as f^-, and $f(\omega+\omega_0)$ as f^+, where f's represent the relevant quantities such as the potential and the plasma susceptabilities. One can simplify this equation for small μ_σ ($\mu_\sigma < 1$) by expanding the Bessel function in μ_σ. This approximation is valid in our experiments. We note that the theoretically obtained threshold for the decay processes which we shall discuss here yields threshold values corresponding to $\mu \ll 1$, so that the small μ approximation is internally consistant.

After the ordering and retaining the terms up to $O(\mu_\sigma^2)$, we obtain an expression for the dispersion relation in the following form:

$$\varepsilon \, \varepsilon^+ \varepsilon^- \left[1 + \sum_\sigma \frac{\mu_\sigma^2}{4} (\chi_\sigma^+ + \chi_\sigma^-) \right] + \varepsilon^+ \varepsilon^- \sum_\sigma \frac{\mu_\sigma^2}{4} (\chi_\sigma^+ + \chi_\sigma^- - 2\chi_\sigma)$$

$$+ \varepsilon \, \varepsilon^+ \left[\sum_\sigma \frac{\mu_\sigma^2}{4} (\chi_\sigma - 2\chi_\sigma^-) - \sum_\sigma \frac{\mu_\sigma}{2} e^{-i\beta_\sigma} \chi_\sigma^- \sum_\sigma \frac{\mu_\sigma}{2} e^{i\beta_\sigma} \chi_\sigma^- \right]$$

$$+ \varepsilon \, \varepsilon^- \left[\sum_\sigma \frac{\mu_\sigma^2}{4} (\chi_\sigma - 2\chi_\sigma^+) - \sum_\sigma \frac{\mu_\sigma}{2} e^{-i\beta_\sigma} \chi_\sigma^+ \sum_\sigma \frac{\mu_\sigma}{2} e^{i\beta_\sigma} \chi_\sigma^+ \right]$$

$$- \varepsilon^- \sum_\sigma e^{i\beta_\sigma} \frac{\mu_\sigma}{2} (\chi_\sigma - \chi_\sigma^+) \sum_\sigma e^{-i\beta_\sigma} \frac{\mu_\sigma}{2} (\chi_\sigma - \chi_\sigma^+)$$

$$- \varepsilon^+ \sum_\sigma e^{i\beta_\sigma} \frac{\mu_\sigma}{2} (\chi_\sigma - \chi_\sigma^-) \sum_\sigma e^{-i\beta_\sigma} \frac{\mu_\sigma}{2} (\chi_\sigma - \chi_\sigma^-) = 0 \quad . \quad (4)$$

One can also express Eq. (4) in terms of $|\mu_\sigma - \mu_\eta|$, the relative drift motion among species σ and η. After some algebra Eq. (4) reduces to the following simple expression:

$$1 + \sum_\sigma \sum_\eta \sum_{\xi=+,-} \frac{|\mu_\sigma - \mu_\eta|^2}{8\epsilon\epsilon^\xi} \left[(\chi_\eta^\xi - \chi_\sigma)(\chi_\eta^\xi - \chi_\eta) + \epsilon\chi_\sigma^\xi\chi_\eta^\xi \right] = 0 \tag{5}$$

where the summation σ and η are over all species, and the summation ξ is over the upper and lower sidebands. Here we let $\mu_\sigma e^{-i\beta\sigma} \to \mu_\sigma$. For a single-ion-species plasma, if the ion drift motion is neglected, Eq. (5) reduces to Eq. (8) of Porkolab.[16] We have also carried out a calculation including terms to $O(\mu_\sigma^4)$, but their inclusion did not significantly alter the result as long as $\mu_\sigma^2 < 1$.

We now consider parametric excitation of electrostatic ion cyclotron waves and drift waves in a two-ion-species plasma.

B. DECAYS IN TWO-ION-SPECIES PLASMA

When there are two types of ions present in a plasma, the relative ion drift motion can excite a new type of instability where both modes are of the kinetic type (i.e. $\omega_1/k_\parallel, \omega_2/k_\parallel < V_{Te}$). This makes parametric coupling among such waves as the electrostatic ion cyclotron waves and drift waves possible. In a single-ion-species plasma, this type of decay has a very high threshold since $\chi_e \sim 1/(k^2\lambda_{De}^2)$ $\sim \chi_e^-$ which makes the dominant coupling term $\chi_e - \chi_e^-$ to vanish [see Eq. (5)]. We now consider two types of instabilities.

1. PARAMETRIC EXCITATION OF ELECTROSTATIC ION CYCLOTRON WAVES:

When both the low frequency and the lower sideband modes are resonant waves (i.e. Re $\epsilon^- = 0 \simeq$ Reϵ), Eq. (5) simplifies to the following form:[7]

$$\epsilon \, \epsilon^- = \left| \frac{\mu_1}{2} - \frac{\mu_2}{2} \right|^2 \left[\text{Re} \, (\chi_2 - \chi_2^-) \right]^2 \tag{6}$$

where, nothing that $\chi_e = 1/(k^2 \lambda_{De}^2) = \chi_e^-$, we have used the equality Re $(\chi_1 - \chi_1^-) = -$ Re $(\chi_2 - \chi_2^-)$. It is apparent from Eq. (6) that electrons play a rather passive role for this decay, and now the relative ion-ion drift motion drives this instability. This is the case for the parametric decay into the two electrostatic ion cyclotron waves.[7] For Eq. (6), we have,

$$\left| \mu_1 - \mu_2 \right| = c \left(\frac{E_0}{B} \right) \left(\frac{k_\perp}{\omega_0} \right) \frac{\omega_0 (\Omega_2 - \Omega_1)(\omega_0^2 + \Omega_1 \Omega_2)}{(\omega_0^2 - \Omega_2^2)(\omega_0^2 - \Omega_1^2)} \quad .$$

The real part of the dispersion relation of the electrostatic ion cyclotron waves can be written in the following form:[17]

$$1 + \frac{1}{k^2 \lambda_{De}^2} - \sum_\sigma \frac{1}{k^2 \lambda_{D\sigma}^2} \sum_{n=1}^{\infty} I_n(b_\sigma) \, \exp(-b_\sigma) \frac{2n^2 \Omega_\sigma^2}{\omega^2 - n^2 \Omega_\sigma^2} = 0 \quad . \tag{7}$$

Here $\lambda_{D\sigma}$ is the Debye length of the species σ, $b_\sigma = k_\perp^2 T_\sigma / (m_\sigma \Omega_\sigma^2)$, and I_n is the modified Bessel's function of the first kind.

In a cold ion, two-ion-species plasma, Eq. (7) simplifies to the following equation:

$$1 + \frac{1}{k^2 \lambda_{De}^2} - \frac{(\omega_{p1}^2 + \omega_{p2}^2)(\omega^2 - \omega_{IH}^2)}{(\omega^2 - \Omega_1^2)(\omega^2 - \Omega_2^2)} \frac{k_\perp^2}{k^2} = 0 \quad , \quad (8)$$

where ω_{IH} is the ion-ion hybrid frequency defined as,[18] (9)

$$\omega_{IH}^2 = \frac{\omega_{p1}^2 \Omega_2^2 + \omega_{p2}^2 \Omega_1^2}{\omega_{p1}^2 + \omega_{p2}^2} = \Omega_1 \Omega_2 \frac{N_1 M_1 Z_1 Z_2 + N_2 M_2 Z_1 Z_2}{N_1 M_2 Z_1^2 + N_2 M_1 Z_2^2} \quad .$$

Here N_i are the partial ion concentrations and Z_i are their charge states such that $\sum_i N_i Z_i = 1$. The wave dispersion relation shown in Eq. (8) predicts two propagating branches, one above each ion cyclotron frequency. The low frequency branch, $\omega_1(k)$ has a resonance at ω_{IH} and the high frequency branch, $\omega_2(k)$ extends to the lower hybrid frequency. Then each branch has a cut-off at the ion cyclotron frequency which is essentially equal to the ion plasma frequency in the present case.[17] Each branch has a cut-off at the respective ion cyclotron frequencies. As an illustration, in Fig. 1 we plot with solid curves the above dispersion relation for a He : Ne = 4:6 plasma. These two branches provide decay pairs for the parametric instability. We also plot the frequency sum of the two modes, $\omega_1(k) + \omega_2(k)$, as a dotted curve. This curve is useful in determining the possible decay pair for a

given pump frequency. In the same figure, we show typical decay pairs for three different values of ω_0/Ω_{He}. As one can see from the figure, there is one unique decay pair for a given value of ω_0/Ω_{He} and the decay is possible for a wide range of ω_0 for $\omega_0 > \Omega_1 + \Omega_2$ (where $\Omega_{He} = \Omega_2$). Writing the cold-ion dispersion relation for each of the decay waves, $\omega_1(k)$ and $\omega_2(k)$, and using the selection rules, Eq. 1, we obtain the following relation for the lower side-band, $\omega_2(k)$,

$$(\omega_2^2 - \omega_1^2)[(\omega_0 - \omega_2)^2 - \omega_1^2] - (\frac{N_1 m_2}{N_2 m_1})(\omega_2^2 - \omega_2^2)$$

$$\times [\omega_2^2 - (\omega_0 - \omega_2)^2] = 0 . \tag{10}$$

Here N_1 and N_2 are the relative ion concentrations, and m_1 and m_2 are the masses of the two ion species, with m_2 being the lighter species. We note that for a given pump frequency and ion species, the decay wave frequency depends only upon the relative ion concentration ratio and the magnetic field strength, and is independent of the plasma density, the electron temperature and the wave number. Hence, it will be relatively easy to check experimentally the selection rules through Eq. (10).

Finally, in a finite length system the threshold is increased due to convective losses. In particular, in a system of length L the threshold is given by[19,20]

$$\gamma_0^2 = V_1 V_2 \left[\frac{\pi^2}{4L^2} + \frac{1}{4} \left(\frac{\Gamma_1}{V_1} + \frac{\Gamma_2}{V_2}\right)^2\right], \quad (11)$$

where

$$\gamma_0^2 = \frac{|\mu_1 - \mu_2|^2 |\chi_2 - \chi_2^-|^2}{4 (\partial\varepsilon/\partial\omega_1) (\partial\varepsilon/\partial\omega_2)},$$

is the growth rate in a uniform system expressed by Eq. (6). Here L is the size of plasma column (which is usually 4-5 cm in our case), $V_{1,2}$ are the group velocities of the two decay modes, $\Gamma_{1,2}$ are their damping rates.

2. PARAMETRIC EXCITATION OF DRIFT WAVES:

When the frequency ω of the low frequency mode is comparable to the linear damping rate, γ^- of the side-band mode, it is necessary to include in the dispersion relation both the lower and upper sideband contributions. Such is the case when we consider decay into ion cyclotron waves and drift waves. Then Eq. (5) can be expressed in the following form:

$$\varepsilon = \left|\frac{\mu_1}{2} - \frac{\mu_2}{2}\right|^2 \left[\text{Re}(\chi_2 - \chi_2^0)\right]^2 \left(\frac{1}{\varepsilon^-} + \frac{1}{\varepsilon^+}\right), \quad (12)$$

where χ_2^0 is the ion susceptability of the sideband mode calculated at the pump frequency. Here we have made an approximation, $\text{Re}\chi_2^- \simeq \text{Re}\chi_2^0 \simeq \text{Re}\chi_2^+$ (since the two sidebands are only a few percent apart from ω_0). For the excitation of drift waves this approximation is easily satisfied in our experiments.

One can solve Eq. (12) using an anologous calculation
which was carried out in Ref. 21. We let $\omega_1 \simeq \omega$ and $\omega_2 \simeq \omega_0$
where ω_1 and ω_2 are the natural frequencies of the plasma.
We are here allowing a possibility of frequency mismatch in
our calculation. In other words, the waves are allowed to
be excited at frequencies which are shifted from their
respective natural frequencies. Expanding ϵ about ω_1 and
ϵ^+, ϵ^- about ω_2, Eq. (12) takes on the following form:

$$i\Gamma_1 + (\omega - \omega_1) = \frac{|\mu_1 - \mu_2|^2 \, [\mathrm{Re}(\chi_2 - \chi_2^0)]^2}{4 \frac{\partial \epsilon}{\partial \omega_1} \frac{\partial \epsilon}{\partial \omega_2}} [\frac{1}{\omega + \delta + i\Gamma_2} - \frac{1}{\omega - \delta + i\Gamma_2}],$$

(13)

where $\Gamma_1 = |\mathrm{Im}\,\epsilon(\omega_1)/(\partial\epsilon/\partial\omega_1)|$, and $\Gamma_2 = |\mathrm{Im}\,\epsilon(\omega_2)/(\partial\epsilon/\partial\omega_2)|$
are the damping frequencies, and $\delta = \omega_0 - \omega_2$ is the frequency
mismatch term. By letting $\omega = x + iy$ in Eq. (13) and separating
the resulting equation into real and imaginary terms, one
can obtain a set of two independent equations. Then in
principle, one can solve for any two unknown quantities.
For a given pump electric field, one can solve for the fre-
quency x, and the growth rate y for certain δ. One can
also solve for the threshold electric field and the fre-
quency x for given δ by letting y=0. The detailed caluclations
are carried out in Appendix A.

From Eq. (A-7) of the appendix, we obtain the following
condition:

$$|\mu_1-\mu_2|^2 = \frac{\partial\varepsilon/\partial\omega_1\,\partial\varepsilon/\partial\omega_2}{[Re(\chi_1-\chi_1^0)|^2}\frac{\Gamma_1}{\varepsilon\;\Gamma_2}\left\{\omega_1^3+2\omega_1(\Gamma_2^2-\delta^2)\right. \tag{14a}$$

$$\left.+\frac{\omega_1^2\alpha^2+(\delta^2+\Gamma_2^2)^2}{[\omega_1/2+(\omega_1^2/4+\alpha^2)^{1/2}]}\right\}\;,$$

$$|\dot{\mu}_1-\mu_2| \approx c\;\frac{E_{o\perp}}{B}\frac{\sqrt{K_r^2+K_\theta^2}}{\omega_o^2-\Omega_2^2}\;\Omega_2\;\;, \tag{14b}$$

and

$$\omega = \frac{\omega_1}{2}+\left[\frac{\omega_1^2}{4}+\frac{\omega_1(\Gamma_2^2+\delta^2)}{2\Gamma_2}\right]^{1/2}\;\;, \tag{15}$$

where $\alpha^2=\Gamma_1(\Gamma_2^2+\delta^2)/2\Gamma_2$, $\delta=\omega_0-\omega_2$, and Γ_1 and Γ_2 are the linear damping frequency for the low frequency and the high frequency modes, respectively. Here Γ_1 is assumed small compared to Γ_2. We have also assumed $\Omega_2 >> \Omega_1$ in deriving Eq. 14(b). Using above equations, for a given δ, one can calculate the threshold and excited frequencies. The excited drift wave frequency ω is up-shifted from its natural frequency ω_1. Equation (14a) shows that for $\delta<0$ or $\omega_2>\omega_0$, the decay is stable.

The dielectric constant for a drift wave in a density gradient can be expressed as,[22]

$$\varepsilon(\omega_1) = 1+\frac{1}{k^2\lambda_{De}^2}+\sum_i\frac{\omega_{pi}^2}{\Omega_i^2}-\frac{1}{k^2\lambda_{De}^2}\frac{\omega^*}{\omega_1} = 0,\quad \tag{16}$$

where we have generalized the results to multi-ion species.
Here $\omega^* = k_\theta V_D$, k_θ is the azimuthal wave number, $V_D = c\, T_e/$
eBL, $L = n/|\partial n/\partial r|$ is the plasma density gradient scale
length, k is the perpendicular wave number, and λ_{De} is the
electron Debye length. From Eq. (16) one can obtain the linear
dispersion relation of drift waves in the following form:

$$\omega_1 = \omega^* \, / \, (1 + k^2\lambda_{De}^2 + k^2\lambda_{De}^2 \sum_i \omega_{pi}^2/\omega_i^2) . \tag{17}$$

The dielectric constant for the electrostatic ion cyclotron
wave is given in the following form:

$$\varepsilon(\omega_2) = 1 + \frac{1}{k^2\lambda_{De}^2} - \sum_i \frac{\omega_{pi}^2}{\omega_2^2 - \Omega_i^2} = 0. \tag{18}$$

where we assumed $T_i = 0$ (which is appropriate to our experi-
ments). Using Eqs.(16) and (18), one can eliminate the term
$1/(k\lambda_{De})^2$ and obtain the following relation:

$$\omega_1 = \omega^* \, \sum_i \frac{\omega_{pi}^2}{\omega_2^2 - \Omega_i^2} \, / \, \sum_i \left(\frac{\omega_{pi}^2}{\Omega_i^2}\right) \frac{\omega_{pi}^2}{\omega_2^2 - \Omega_i^2} . \tag{19}$$

Equation (19) shows that in order to satisfy the wave number
matching condition, ω_1 has to be less than ω^* if ω_2 (or ω_0)
is above Ω_i. However, as shown by Eq. (17), this is precisely
the condition for drift waves to exist, and one can conclude
that the wave number matching condition can be satisfied
for a wide range of plasma parameters as long as the pump
frequency is above the ion cyclotron frequency.

If we include collisions of electrons with ions and
neutrals, drift wave can become more unstable. The electron
destabilizing term for drift waves was derived in Ref. 23
from the kinetic equations, and the results can be written
in the following form:

$$\chi_e = \frac{1}{k^2 \lambda_{De}^2} \left\{ \frac{1 + [(\omega - \omega^* + i\nu_{e0})/(k_z V_{Te})] \ Z(\zeta)}{1 + i[\nu_{e0} / (k_z V_{Te})] \ Z(\zeta)} \right\}. \qquad (20a)$$

Here $\zeta = (\omega + i\nu_{e0})/(k_z V_{Te})$, $V_{Te} = \sqrt{2T_e/m_e}$, ν_{e0} is the electron-
neutral collision frequency, k_z is the parallel wavelength,
and Z is the plasma dispersion function. We note that Eq. 20(a)
includes both electron Landau damping and electron-neutral
collisions. For $|\zeta| \ll 1$ (collisionless or the Vlasov limit),
Eq. 20(a) reduces to the following simple form:

$$\chi_e = \frac{1}{k^2 \lambda_{De}^2} \ [1 + i \sqrt{\pi} \cdot (\omega - \omega^*)/(k_z V_{Te})] \qquad (20b)$$

For $|\zeta| \gg 1$ (collisional limit), Eq. 20(a) can be written in
the following form:

$$\chi_e = \frac{1}{k^2 \lambda_{De}^2} \cdot \left[\frac{1 - i \ 2 \ \omega^* \nu_{e0}/(k_z V_{Te})^2}{1 - i \ 2 \ \omega \nu_{e0}/(k_z V_{Te})^2} \right]. \qquad (20c)$$

Equation 20(c) can be also derived from fluid theory. For our
experimental parameters, typically $|\zeta| \approx 2.0$, which is in the
transition regime from the collisionless to the collisional
limit. However, an exact numerical solution of Eq. 20(a)
gives a solution which is very close to that of the collisional
case (Eq. 20(c)) to within 10%.

C. RELATIVE AMPLITUDE OF THE SIDEBANDS

Since we now have the dispersion relation of the parametric coupling which relates μ_σ to plasma susceptabilities, by going back to Eq. (3) it is possible to calculate the relative amplitude of the sidebands, ϕ^-/ϕ^+. This is a typical eigen-value-eigenvector problem. Although from such an analysis the ratio of ϕ^-/ϕ^+ can be obtained, the absolute value of the eigenvector can be obtained only from a nonlinear theory of saturation. In Appendix B we derive an expression for the relative fluctuation amplitude of the upper and lower sidebands ϕ^-/ϕ^+.

III.   EXPERIMENTAL SET UP AND MEASUREMENT TECHNIQUES:

   A.   L-4 DEVICE

   A schematic of the L-4 device is shown in Fig. 2.   L-4
is a steady-state linear device with an approximately 230 cm
uniform magnetic field region with a steady-state field strength
of up to 4.2 kG, and a spatial field ripple of 0.5%.   The
typical base pressure of the device is 2-5 x 10^{-8} torr.   The
plasma is produced by a hot tangsten filament plasma source[24]
located at the one end of the device, as shown in Fig. 2.   The
filaments are heated to thermionic emission temperatures, and
the emitted electrons are accelerated by a bias voltage applied
between the filaments and the chamber to ionize the background
neutrals.   The magnets are placed on the chamber wall to confine
the primary electrons.   An auxilary coil is used to control
the convergence of the magnetic field lines which can in turn
change the plasma profiles, and also smoothes out the density
inhomogeneity which can be present in this type of plasma source.

   For the background gasses we have used He, Ne, Ar, and
Kr with a typical filling pressure of $P = 0.8 - 10$ x 10^{-4} Torr
in the source region.   Due to a differential pumping effect
provided by the pump at the opposite end of the device, the
filling pressure is about a factor of two lower in the experi-
mental region than in the source region.   We have used noble
gasses in our experiments since in other gases such as hydrogen,
various ion species such as H_1^+, H_2^+, H_3^+, may be produced.[25]

A plasma with the desired density and concentration ratio is produced by properly monitoring the inflow of each of the neutral gases.

The plasma measurements are carried out mainly by using radially and axially moveable probes. Axial scanning is possible at almost any radial position. A Langmuir probe is used for measuring n_0 and T_e.[26] The RF probes, usually T-shaped, are used for measuring the wave length of various waves. A ceramically shielded double probe is used to measure the pump RF electric field. An RF double probe is used to measure the azimuthal wave length. In addition to the probes, we have used electron and ion energy analyzers, and an optical multi-channel analyzer (Grated OMA System, Princeton Applied Research Inc.).

The measured plasma parameters are as follows: The plasma density, $n_0 \leq 3 \times 10^{10}$ cm^{-3}; the electron temperature, $T_e \approx 2$-5 eV; the ion temperature, $T_i < 1/10$ eV; the plasma drift velocity ≈ 0.1 C_s; and the plasma density fluctuation, $\Delta n/n = 1$-2% at the center and 2-5% at the edge of the plasma. The plasma density was measured by a Langmuir probe ion saturation current which was calibrated by the resonance cone propagation of the electron plasma wave.[27] The electron temperature was determined from the measured dispersion relationship of a linearly propagated ion acoustic wave. The magnetic field was measured by the NMR technique to 0.5% accuracy. The ion concentration ratio was measured by the

combined spectroscopic-Langmuire probe techniques and also by the linear propagation of the electrostatic ion cyclotron waves. Since the ion concentration measurements are important and somewhat involved, we describe them in detail in the next section.

B.   ION CONCENTRATION MEASUREMENT.

In order to carry out a quantitative study of multi-ion-species effects, one of the important plasma parameters to know is the ion concentration ratio. We present here two independent methods to measure the concentration ratio and compare them for consistancy. One method uses spectroscopy and Langmuire probe techniques and the other method utilizes the wave dispersion relation of the electrostatic ion cyclo-tron wave which can be readily measured with a good accuracy in a laboratory plasma.

1.   Spectroscopic-Langmuire Probe Techniques.

We shall consider here a plasma consisting of helium and neon ions. For our relatively low temperature weakly ionized plasma the ions are singly ionized and therefore the only ions to be considered here are H_e^+ and N_e^+. Then from the charge neutrality condition, the combined density of the helium and neon ions is equal to that of the electrons (i.e. $n_{He} + n_{Ne} = n_e = n_o$). Thus, in order to obtain the ion concentration ratio, one needs to measure the density of the electrons and at least one of the ion species. This method utilizes the fact that a specific spectral line intensity (namely $5015A^o$ for He and

5852Å for Ne) emitted by the plasma is related to the density
of that particular ion species in the plasma, and the electron
saturation current is related to the electron density. We
then calibrate these quantities with the ion saturation current
using pure helium plasma and pure neon plasma. We note that
this method uses the ion saturation current only as a common
scale to relate the densities among ions and electrons.
Therefore this method is not subjected to errors which are
often introduced when one converts the ion saturation current
into the ion density[26].

In a pure helium plasma, we calibrated the helium line
(5J15Å) intensity and the electron saturation current with
the ion saturation current. The helium line is well under-
stood, and in a low density plasma such as ours this line
provides good indication of the helium ion density.[28-31]
We discuss such a relation in Appendix C. Then in a pure
neon plasma, we calibrated the neon line (5852Å) intensity
and the electron saturation current with the ion saturation
current. Such calibration curves are shown in Fig. 3(a)
and 3(b). These four calibration curves show good linear
relationship. It should be noted that due to the presence
of magnetic field, the ratio of the electron saturation
current to the ion saturation current, as shown by Fig. 3(b)
is not simply the square root of the ion to electron mass
ratio. However, the slopes of the two electron saturation
currents show a correct dependence upon the square root of

the ion mass ratio ($m_{He}:m_{Ne} = 1:5$). The non-zero electron current (even when the plasma density is reduced to zero) is due to the primary electrons from the plasma source.

In Fig. 3(a), the neon curve shows a non-linearlity in the high density side ($n_{Ne} \gtrsim 2.0 \times 10^{10} cm^{-3}$); however, in the present experiment the concentration measurement was done for $n_{Ne} \lesssim 10^{10} cm^{-3}$ where the curve is linear. Using these calibration curves, we obtained the ion concentration ratios of the helium-neon plasmas by measuring the neutral line intensities and the electron saturatior currents. We note that the ion concentration ratio can be obtained either by comparing the electron saturation current with one of the neutral line intensities, or by comparing the intensities of the two neutral lines. The measured ion concentrations are found to have better than 20% consistancy in most cases.

Since the calibration curves are prepared in a single-ion-species plasma, we have considered the effect on such calibration curves when two-ion-species are mixed. There are two possible processes which may affect the ion calibration curves: these are the charge-exchange between an ion and a neutral atom of a different species, and recombination. The charge-exchange process can increase the density of one ion species while decreasing the other. However, in a low temperature plasma such as ours ($T_i < 0.1$ eV) the cross sections for such charge-exchange process turned

out to be extremely small and therefore could be neglected.[32,33] The recombination can reduce the densities of both ion species and depends upon the plasma density. In our low density plasma with almost no plasma confinement, such a process is very slow and can be neglected. Therefore, we concluded that the calibration curves are still relavant even when the ions are mixed.

2. Electrostatic Ion Cyclotron Wave Propagation Method.

Due to its strong dependence on the ion concentration ratio, the electrostatic ion cyclotron wave can also be used to measure the concentration ratios. The wave dispersion relation in a two-ion-species plasma can be written in the following form:

$$k^2 = \frac{1}{T_e} \left[\frac{N_1}{m_1 \, (\omega^2 - \Omega_1^2)} + \frac{N_2}{m_2 \, (\omega^2 - \Omega_2^2)} - \cdots \right]^{-1} . \quad (21)$$

Here we neglected the finite Larmor radius effect and assumed $\omega_{pi} \gg \Omega_i$. By experimentally measuring the wave number of the linearly propagated electrostatic ion cyclotron wave for various values of ω, it is quite straight-forward to determine N_1 (or $N_2 = 1-N_1$) and T_e from Eq.(21). A schematic of the experimental set-up is shown in Fig. 4 (a). The wave is launched from a 1" x 1" square grid structure aligned parallel to the magnetic field. The excited wave, which propagates perpendicular to the magnetic field, is detected by a radially moveable T-shaped probe. The detected signals are processed by standard interferometry techniques and

plotted on a chart-recorder as a function of the probe
position. We observe that the measured wave-lengths depend
strongly on the ion concentration ratios. One can compare
this propagation method with the spectroscopic-Langmuire
probe method by plotting the measured wave length as a
function of the measured ion concentration ratio. Such
a plot is shown for the fixed wave frequency and magnetic
field in Fig. 4(b). The solid curve corresponds to the
theoretical dispersion relation of the cyclotron wave
derived from Eq.(21). The agreement between the theory
and experiment is quite good. From such measurements, we
conclude that the two measuring techniques are consistant.
The propagation method can also indicate the spatial
variation of the ion concentration in a plasma. Within
the experimental uncertainty in our experiment, the
measured ion concentrations are observed to be uniform
throughout the plasma column.

C. RF SYSTEM

In order to study non-linear processes, it is neces-
sary to induce a uniform oscillating electric field of
sufficiently large amplitude inside the plasma. Because
of the low frequency nature of the pump electric field,
$\omega_0 = O(\Omega_i)$, the electric fields produced by an electrostatic
means of excitation, such as using wires, grids, parallel
plates etc., cannot penetrate sufficiently deeply into

the plasma except by coupling to a normal mode of the plasma.
However if an electrostatic wave is used for a pump wave,
the pump wavelength would be comparable to that of the wave-
length of the decay waves and probably would not simulate tokamak
ICRF heating experiments very well.[1] An ideal pump would be an
electromagnetic wave, such as the magnetosonic wave, since
it usually has a long wavelength compared with that of the
decay waves which are electrostatic in nature. Even though
electromagnetic modes do not exist in a plasma with $n_o \approx 10^{10}$
cm^{-3}, one can show that the evanescent electric field pro-
duced by an induction coil would penetrate into such a plasma
across the magnetic field line with a scale length of $|k_{\perp}|^{-1}$
$\approx |k_{\shortparallel}|^{-1}$, which can be chosen to be much larger than the
plasma column size,d. Therefore, by using an external induction
coil, it is possible to impress long scale-length evanescent
electric fields inside the plasma, and this is the technique
we chose for generating a pump electric field.

A circuit diagram of the RF system is shown in Fig. 5(a).
The system utilizes a 3 kW steady state RF oscillator as a
source. The oscillator frequency can be varied in the range
of 2-30 MHz, and it has both an "in-phase" and "out-of-phase"
output terminal. This oscillator is properly matched to the
RF induction coil by a matching network. We note that the
RF coil and the matching network consist of identical
sections which can be driven in-or-out-of-phase depending
upon the desired current configuration. The matching net-
work together with the induction coil functions as an L-C

resonant circuit with a Q-factor of about 100. When
matched properly, an RF current of up to 40 amperes can
be induced in the RF coil. The inductances and the capa-
citances are chosen so as to satisfy the L-C resonant con-
dition $1/LC = \omega_0^2$, and also to match the impedence seen
from the oscillator, namely $z \approx 200$ ohms. The loading
resistance is measured to be about 0.5Ω. Due to the low
plasma density the plasma loading is observed to be
negligible. The current through the induction coil is
monitored by a wideband current transformer, and the voltage
across the coil is monitored by a high voltage probe.

The schematic RF coil structure is shown in Fig. 5 (b).
The RF coil (1/8" x 1/8" copper bar stock) is embedded in
a machinable ceramic structure which shields the coil from
the plasma and from the neighboring turns. The multi-turn
coil configuration was chosen to increase the induced electric
field for a given pump power. This configuration also re-
duces the power handling requirement for the capacitors
used in the matching network. A Faraday shield is placed
on the inner walls of the ceramic structure to shield out
the electrostatic field generated by the inductive potential
drop along the coil. The structure has three radial access
port openings, each of one inch square, and an axial gap
for the axial probe. These accessibility features are
particularly important for the measurement of the wavelengths
of the decay waves.

In order to introduce flexibility in our pump electric
field, we have designed the RF coil structure so that it

can induce either an m=0 or an m=1 type electric field in the plasma (where m is the azimuthal mode number). The m=1 type coil induces a large uniform electric field at the center of the plasma column, whereas the m=0 type coil produces a radially varying electric field which vanishes at the center of the plasma column. This is confirmed by the measurements of the electric field which will be described shortly. There-fore, in our experiments where a large uniform electric field near the center of the plasma column was needed, we used the m=1 coil configuration almost exclusively.

The electric field produced by the coil structure can easily be calculated from Maxwell's equations.[34] In our cal-culations we have numberically summed up the contribution of each coil segment to give a realistic electric field profile. The presence of the vacuum chamber which produces image currents, was estimated to affect the electric field by less than 20%. In Fig. 6, we show a two dimensional electric field profile calculated for the m=1 current configuration. As expected, the figure shows a large uniform electric field region in the center of the structure. The multi-turn nature of the coil tends to spread out the current, and thus, reduces the singular nature of the coil current.

Although the electric field generated by the coil can be calculated for any given current configuration, it is impor-tant to measure it experimentally. For this reason, we have constructed a double probe which was ceramically shielded to

eliminate plasma effects, such as plasma fluctuations. This probe was calibrated via a parallel plate capacitor generating a known electric field. Using this double probe, we have measured the RF electric field actually produced by the RF induction coil both with, and without the plasma. The result of such a measurement is shown in Fig. 7(a). The calculated theoretical value is plotted for comparison. The electric fields have indeed penetrated inside the plasma with a good uniformity at the center. The somewhat higher values for the measured electric field with the plasma may be due to the plasma sheath formed at the probe-plasma boundary. Since the expected accuracy of the absolute values of such measurements is typically within a factor of two, the agreement is quite reasonable. The increase of the measured electric field at the edge of the plasma near the induction coil may be due to imperfection of the Faraday shield which permitted some leakage of the electrostatic field which we neglected in our calculation. However, in our experiments the decay instability is excited in the region of the uniform field. The measured electric field versus the induction coil current is shown in Fig. 7(b); this shows a good linear relation of the two quantities, in accordance with the theory.

By using the interferometry set-up, we have searched for electrostatic waves at the pump frequency. This was motivated by a report of a linear excitation of the electrostatic wave via a mode conversion process at the lower hybrid resonance layer by an $m = 0$ induction coil.[35] However, our

search proved to be negative and thus we concluded that our pump electric field can indeed be described by the dipole approximation (i.e. $\vec{k}_0=0$). This conclusion is further supported by the measurements of the decay wavelengths which always show that the wave number matching condition, $|\vec{k}_1|=|\vec{k}_2|$, is satisfied in our experiments.

IV. EXPERIMENTAL RESULTS:

  A. PARAMETRIC EXCITATION OF ELECTROSTATIC ION CYCLOTRON
      WAVES:

      In this section, we present experimental studies
of parametric excitation of the electrostatic ion cyclotron
waves. The experiments were carried out in the following range
of plasma parameters: the magnetic field, $B_0 \lesssim 4.2$ kG; the
plasma density, $N_0 = 10^9-10^{10}/cm^3$; the temperatures, $T_e =$
3-5 eV and $T_i < 0.1$ eV; and the neutral gas filling pressure
in the experimental region, $P = 1.0 \times 10^{-4}$ Torr.

      1. Linear Wave Study:

      First, we would like to present results from the
linear propagation of electrostatic ion cyclotron waves
in a helium-neon plasma. The interferometry set-up
is shown in Fig. 4 (a), and as an exciter a 1" x 1" square
grid was used. This measurement was necessitated by the
lack of any experimental measurements of the linear
dispersion relation of electrostatic ion cyclotron waves
in a two-ion species plasma (even though various groups
have experimentally investigated the ion cyclotron waves
in a single-ion-species plasmas[36-38]. We were especially
interested in the resonance behavior near the ion-ion
hybrid frequency. The only related work is the linear
propagation of the ion acoustic waves in a two-ion species
plasma.[39] Using the above set-up, we have mapped the wave
dispersion relation for a whole range of ion concentration
ratios. The results of such measurements are shown by

the dots in Fig. 8.   The solid curves are the theoretical
dispersion relations calculated using Eq.(7) for T_i = 1/40 eV
and for the ion concentration ratio as indicated. As ex-
pected the dispersion relations show one propagating mode
above each ion cyclotron frequency (except for the pure neon
case where the dispersion relation is continuous). The pro-
pagation of the mode above the helium ion cyclotron frequency
was relatively straight forward for all concentration ratios.
The propagation of the low frequency mode was much more difficult
especially near the ion-ion hybrid frequency, and also for
the larger helium ion concentration.   In fact, we could not
observe the propagation of the mode for helium concentra-
tions above 60%. Although the damping is heavy, the tendency
for the wave to approach the resonance near the hybrid
frequency appears to be reasonably clear. We also observed
a rather heavy wave attenuation near the second harmonic
of the ion cyclotron frequency. Over all, we conclude
that the agreement between the theory and the linear pro-
pagation measurements is good.

  2.   Parametric Instability Excitation.

  The experimental investigation of parametric excitation
of the electrostatic ion cyclotron waves was carried out
using the RF-system which was described in detail in Section
III, Part C. As the pump electric field was increased

above a certain threshold level, we observed a sudden

onset of parametric decay at the center of the plasma

column. This decay was observed to occur only when the

plasma contained two types of ions. This is in agreement

with the theoretical prediction that a relative ion drift motion

is required for   parametric excitation. In Fig. 9, we show a

typical radial density profile, the pump electric field pro-

file, and the interferometry traces of the decay waves. As

shown in the figure, the wave number matching condition

$|\vec{k}_1| = |\vec{k}_2|$ was always found to be satisfied within the

experimental uncertainty. A typical decay frequency

spectrum obtained in a helium-neon plasma is shown in

Fig. 10. As expected from the theory, the decay waves

were excited above each ion cyclotron frequency, and the

frequencies were found to vary with the magnetic field and

the relative ion concentration ratio. (We note that

similar decay waves were also observed in helium-argon

and helium-krypton plasmas.) The subsequent data pre-

sented here were obtained in a helium-neon plasma. From the

variation of the decay frequencies and wavelengths with

the magnetic field strength, and a dependence of the frequencies

upon the ion concentration ratio, the decay waves were

identified to correspond to the two branches of the electro-

static ion cyclotron waves as predicted by theory.

In Fig. 10, the theoretical dispersion curves of ion

cyclotron waves(given by Eq.(8))in a helium-neon plasma

with He:Ne = 4:6 is shown by the solid curves. In the
same figure, the experimentally measured values of $\omega(k)$,
as determined by interferometric measurements of the
wave numbers of the decay waves, are shown by the cir-
cles. We see good agreement between the experimentally
measured values and the cold ion plasma theory, except
near the harmonics of the ion cyclotron frequency. In
order to explain this deviation from the cold ion plasma
theory, we have numerically calculated the hot-plasma
dispersion relation given by Eq.(7), including finite
ion Larmor radius effects. In Fig. 10, we show such
theoretical plots with dotted lines for various ion
temperatures which may be expected in our device. We
see that the best agreement between theory and experiment
is obtained by assuming $T_i=1/40$ eV (or T_i approximately
equal to room temperature). We note that in the two-ion
species plasmas the gap in the dispersion curves near
the second ion cyclotron harmonic frequency is considerably
enhanced by the finite ion Larmor radius effects (especially
for the lighter ion species). Thus, these experiments pro-
vide an interesting technique to estimate the low ion temp-
erature that characterize plasma devices such as ours.

Another noteworthy feature of the parametrically
obtained dispersion relation shown in Fig.10 is the branch
near the ion-ion hybrid frequency, where the dispersion
relation shows a strong resonance behavior. We note that

the linear propagation of the wave becomes increasingly difficult as the frequency approaches the hybrid frequency, and will not propagate at all for $kC_s/\Omega_{He} > 2.0$. This is due to the fact that the wave spacial damping rate, $\text{Im } k \simeq \nu/v_g$, becomes large near the resonance where $v_g \cdot 0$. On the other hand, for parametric instability, the pumps electric field is constantly pumping energy into the decay modes to offset such wave dissipation processes. Otherwords, above the threshold electric fields, the plasma becomes amplifying medium for the decay waves. Furthermore due to the selection rules (Eq. (1)), the excited decay modes are relatively coherent. Therefore, the modes near the resonance frequency could be excited parametrically, and the interferometric measurement of such modes were possible. We shall call the present mode near the ion-ion hybrid frequency, "the kinetic ion-ion hybrid mode" since in our plasma it occured in a hot electron plasma (i.e., $\omega/K_\parallel < V_{Te}$ as opposed to the Buchsbaum mode which occurs for $\omega/K_\parallel \gg V_{Te}[40]$).

In Fig. 11(a) we have plotted the experimentally observed decay frequencies, normalized by a unit of helium ion cyclotron frequency, for various ratios of ion concentration as a function of the magnetic field. The solid lines are the theoretical curves obtained from Eq. (10). We see that the experimentally observed values are again in a good agreement with the theoretical curves. In accordance with the predictions of the theory, the decay spectra disappeared when either of the ion species was removed from the experimental region.

In Fig. 11(b), we show the experimentally observed
threshold values of pump electric field E_o as a function
of the normalized wave number, kC_s/Ω_{He}. The theoretical
threshold curve for the decay instability was calculated
from Eq.(11) including terms for electron Landau damping,
ion-ion collisions among the differenc ion species, and
ion-neutral collisions,[32] as well as finite ion Larmor
radius effects in the real part of the plasma dielectric
constant. For our experimental parameters, ion Landau
damping and ion cyclotron damping are negligible. Ion-
ion collisions among different ion species become signi-
ficant for relatively high-density cold ion plasma. For
our experimental parameters, their contributions are
significant, and hence, they are appropriately included
in the threshold calculations. The effect of the ion-
ion collisions among ions of different species and the
ion-neutral collisions upon the electrostatic ion cyclotron
wave has been calculated in Appendix D. Electron Landau
damping is estimated from the measured parallel wavelength
of the decay waves, which are typically 4 to 5 cm. The
comparison of the experimentally measured values (using
the calibrated RF probe) with the theoretically obtained
values shows a good agreement, well within the experimental

uncertainty which is typically a factor of 2. We note that the systematic deviation between theory and experiment for $kC_s/\Omega_{He} \gtrsim 2.0$ may be due to viscous ion damping which was not included in our calculations.[23]

B. PARAMETRIC EXCITATION OF DRIFT WAVES:

1. Frequency Spectrum

The drift waves have received considerable interest due to their possible roles on the confinement of laboratory plasmas. In this section, we present experimental studies of parametric excitation of drift waves when an RF electric field near the ion cyclotron frequency is applied to the plasma. The observed decay is driven by the ion-ion drift motion and thus it occured only in a two-ion-species plasma. This parametric process excites low frequency drift wave and an ion cyclotron wave. This type of instability may become important during radio frequency heating near the ion cyclotron frequency in multi-ion species plasmas such as a deuterium-tritium fusion reactor plasma. The experimental parameters used in the experiments were as follows: the magnetic field $B \lesssim 4.2$ kG, $f_{ci}(He) < 1.6$ MHz, the plasma density at the drift wave region $n \approx 5 - 10 \times 10^9$ cm^{-3}, the temperatures $T_e = 2.5 - 5$ eV and $T_i < 0.1$ eV, the neutral gas filling pressure in the experimental region $P \approx 3 - 6 \times 10^{-4}$ Torr. We used the same RF induction coil structure and the RF system which were described in Section III, Part C. In order to impress a radially uniform electric field with

field strengths of up to 15 V/cm in the plasma, the $m = 1$ configuration was used.

As the pump power was increased above a threshold level, we observed a sudden onset of parametric decay in the region with large density gradients when sufficiently large fraction of second ion species was added to the plasma. In Fig. 12(a) we show typical radial profiles of the plasma density, the decay wave amplitude, and the electron temperature. As shown in the figure, the decay waves are localized at the plasma density gradient well inside the plasma column. In the experiments we noted that the radial profiles of the decay waves (the low frequency mode and the sideband modes) are quite similar, and show radially a standing wave pattern. The electron temperature profile was obtained by propagating the electrostatic ion cyclotron waves in the vicinity of the decay region. As shown by the figure, the electron temperature is reasonably constant throughout the center of the plasma column, including the decay region, and falls off only at the outer edge of the decay region. From such measurement, we concluded that the temperature gradient effect is much smaller than the density gradient effect in our experiments. In Fig. 12(b), a typical decay frequency spectrum observed in a helium-neon plasma is shown (we also observed similar decay spectra in helium-argon as well as helium-krypton plasmas.). The following data and analysis were

done in a helium-neon plasma. We note that the parametric
decay spectra for the present decay always show the upper
sideband amplitude to be comparable to that of the lower
sideband. This is in agreement with the result obtained
in Appendix B where, for the drift wave excitation, $|\phi^-|/$
$|\phi^+|$ is typically 1.1. This observation reaffirms the
necessity of including the contribution of the upper side-
band in the dispersion relation and the threshold condition.

For a fixed pump power, the decay amplitude is observed
to vary with the ion concentration ratio and the magnetic
field strength. In Fig. 12(c) , the observed decay amplitude
is plotted as a function of the ion concentration ratio with
the magnetic field as a variable parameter. Although the
neighboring drift modes were successively excited as the plasma
parameters were changed, in Fig. 12(c) we show only the
dominant decay mode. In this plot, the pump electric field
is held constant at $E = 8v/cm$ and the pump frequency at 2 MHz.
As shown in the figure, the decay region moves systematically
with the magnetic field and the ion concentration ratio.
The decay spectrum goes away when either of the ion species
was removed which is in agreement with the theory. We note
that near threshold conditions, for a given ion concentration
ratio , as the magnetic field was varied, the density, tempera-
ture and density gradient showed little change during these
measurements . Therefore we could exclude the possibility
that the drift waves are excited by a simple change in the
plasma parameters such as the density gradient.

2. Decay Wave Identification

In order to understand the systematic variation of the excited wave amplitude, it was necessary to investigate the nature of the decay waves in more detail. Using interferometric techniques, we have measured the parallel, radial, and azimuthal wavelengths of the decay waves. The parallel wavelength ($\lambda_{2\shortparallel}$) for the lower and upper sidebands are 15-16 cm, which is the same as the scale-length of the pump, and $\lambda_{1\shortparallel}$ for the low frequency drift wave is approximately 450 cm (about twice the machine length). This long wavelength was measured by placing a set of five RF probes which were aligned to the same magnetic field line and placed at various axial locations. The radial wavelengths were obtained from the amplitude profile of the decay waves which were standing waves in the radial direction; typically $k_r \approx 9.6$ cm^{-1}. The azimuthal wavelengths were measured by a rotative double probe, and for the dominant drift mode, $k_\theta \approx 4.2$ cm^{-1} (which corresponds to the azimuthal mode of m=6), and for the sideband mode, we find $k_\theta \approx 4.8$ cm^{-1} (m=7); thus, taking $k_\theta \approx 0.6$ cm^{-1} for the pump (m=1), we find that the selection rule in the θ direction are satisfied. From such measurement, we have varified that low frequency mode was indeed a drift wave and that the sideband mode was the electrostatic ion cyclotron wave.

By knowing the decay waves and their dispersion relations, one can understand the systematic variation of the excited decay amplitude as shown by Fig. 12(c). For a fixed pump frequency, the frequency of the electrostatic ion cyclotron wave is also fixed (since the drift wave frequency is negligibly small).

Since the wave number of the decay waves are fixed by the wave number matching condition, and since the wave number of the drift wave can not change as long as the mode number and the plasma column profile do not change, the wave number of the ion cyclotron wave can also be regarded as a constant. Therefore in order to satisfy the wave dispersion relation as shown by Eq. (8), for constant ω and $\vec{k}$ the ion concentration ratio has to change with a change in the magnetic field strength. For example, as the neon concentration is being increased, in order to keep ω and $\vec{k}$ constant, the magnetic field has to be increased to make Ω_i closer to ω. In Fig. 12(c), we show with a dotted line the corresponding curve computed from Eq. (8) (using the experimental plasma parameters). Considering the simplicity of the theory, the dotted line roughly corresponds to the location of the decay region in the magnetic field and the ion concentration ratio parameter space. To explain the systematic deviation between such a theory and experiment, it is necessary to go into more detailed theory which takes the frequency mismatch term δ into account, as shown by Eq. (14). We shall discuss this in our threshold analysis of the present decay process.

In Fig. 13 the dots show the observed drift wave frequencies as a function of the magnetic field for various ion concentration ratios. In obtaining these data we fixed the RF electric field at $E = 8$ V/cm. The observed frequency pattern shows that for the higher values of the magnetic

field and the helium ion concentration ratio, the corresponding observed frequency is also higher. This is in a qualitative agreement with the drift wave dispersion relation as given by Eq. (17).

In Fig.14 (a), we plot with dots the excited drift wave frequency as a function of the ion concentration ratio. For each ion concentration ratio, the magnetic field is adjusted so that the drift wave frequency is at the threshold minimum. The solid curve in the same figure shows the corresponding theoretically obtained drift wave frequency. The shaded region around the theoretical curve represents a region of uncertainty due to some experimental uncertainty in the plasma parameters which were used in the theory. From such a plot, we conclude that the observed drift wave frequency agrees reasonably well with the one predicted by the theory. In particular, the quantitative dependence of the drift wave frequency upon the ion concentration ratio shows good agreement with theory.

We have also considered the effect of radial DC electric field E_{DC} which can exist in the density gradient region of our plasma. It can be shown from the fluid equations that the radial DC electric field induces an azimuthal ion rotation of $V_0 = cE_{DC}/B$. This ion rotation causes the drift wave frequency to be Doppler shifted by $\Delta f = k_\theta V_0$. One can estimate such a DC electric field by using the ambipolar diffusion equations which can be expressed in the following form:

$$\vec{E}_{DC} = -\frac{T_e \nu_{e0} m_e - T_i \nu_{i0} m_i}{e\nu_{e0} m_e + e\nu_{i0} m_i} \frac{\vec{\nabla} n}{n}$$

$$\frac{T_i}{e} \frac{\vec{\nabla} n}{n} \quad \simeq \quad -0.1 \ V/cm \ \hat{r},$$

(22)

where ν_{e0} and ν_{i0} are electron-neutral and ion-neutral collision frequencies. In our plasma with $B \simeq 3.5$ kG and $k_\theta = 4.2$ cm^{-1}, the DC electric field $\vec{E}_{DC} = -0.1$ V/cm $\hat{r}$ would produce an upward shift in the drift wave frequency of $\Delta f \simeq 2$ kHz. Therefore, this introduction of the DC electric field would explain the systematic frequency deviation between the observed drift wave frequency and the calculated frequency in Fig.14(a) which shows $\Delta f \simeq 2$kHz in the right direction. We note that in deriving Eq. (22), we did not include the effect of the plasma source which may introduce some additional DC electric field in the plasma.

One can also estimate the electric field by experimentally measuring the floating potential V_f and the electron temperature T_e, and using the relation:[41]

$$\vec{E}_{DC} = -\frac{\partial V_f}{\partial r} \hat{r} - \frac{2.303}{e} \frac{\partial T_e}{\partial r} \log[\sqrt{m_i/m_e} \ \alpha] \ \hat{r} \qquad (23)$$

where α is a correction factor due to the magnetic field and the probe geometry which in our case $\alpha \approx 0.25$. The value of α was estimated experimentally by comparing the ion and electron saturation currents. We note that since

is an argument of a log function and $\sqrt{m_i/m_e}$ is a large number, the equation is only weakly depending on the value of α. In our experiments, we find that the values of T_e and V_f are nearly constant in the drift wave region and then decrease rapidly at the very edge of the plasma which is located outside the drift wave region. In the drift wave region, typically, $1/e \cdot \partial T_e/\partial r = -0.5$ V/cm and $\partial V_f/\partial r = 1.5$ V/cm. Using such values in Eq. (23), the terms in the right hand side of the equation nearly cancel each other and Eq. (23) then gives $\hat{E}_0 = 0.0 \pm 0.4$ V/cm $\hat{r}$. This value of the electric field is consistant with that of the theoretical estimate. Therefore, the estimated electric field strength is consistant with the experimentally observed value. However, the accuracy of such estimate is not good enough to qualitatively include in the theory.

3. Threshold Condition.

In order to determine the excitation mechanism for this decay, using the experimental parameters, we calculated the threshold electric field using Eq. (14). For the imaginary part of the sidebands dielectric constant, we included the ion-neutral and the ion-ion collisions, and electron Landau damping. For the low frequency drift wave, we included the ion-neutral and the electron-neutral collisions and electron Landau damping. As shown in Appendix D, in our experiments ion-ion collisions for drift waves are negligible as compared with ion-neutral collisions. The electron destabilizing term for drift waves is shown by

Eq. (20-a) in terms of $\xi = (\omega + i\gamma_{eo})/(k_z V_{Te})$. For our experimental parameters, typically $|\xi| \approx 2.0$, which is in the transition regime from the collisionless to the collisional limit. However, an exact numerical solution of Eq. (20-a) gives a solution which is very close to that of the collisional case (Eq. (20-c))[41] to within 10%, even though $|\xi| \approx 2.0$.

In Fig. 13, we plot the theoretical threshold contours with solid and dotted curves for various pump electric fields (as labeled). The shaded region is a parametrically stable region which is predicted by the theory ($\delta=\omega_0 - \omega_2 < 0$). The region bounded by the threshold contour is a region of expected decay activity for the corresponding pump electric field. As shown by the figure, the experimentally observed decay region represented by the dots (E = 8 V/cm) agrees quite well with that of the theory. Experimentally, we observe that this decay region shrinks as one decreases the RF electric field, in accord with the theoretical prediction. We note that the elliptic nature of the threshold contour curves shown in Fig. 13 is due to the inclusion of the upper sideband term and the frequency mismatch term in the calculation.

In Fig. 14(b), we plot with dots the experimentally measured threshold electric field as a function of the ion concentration ratio. The corresponding theoretical threshold is plotted in the same figure which shows good

agreement with the experimentally measured threshold.
We note that the threshold rapidly increases as one of
the ion species is depleted.

  4. Coupling to Naturally Occuring Drift-Waves.

  We have so far discussed those drift wave (m=6, k=10.5cm^{-1},
f = 25 - 40 kHz) which were observed to be parametrically
excited by the pump electric field. These drift waves are
naturally stable in our device and can be excited only
when the pump RF electric field exceeds the threshold
value in a two-ion-species plasma. However, we note that
there are some naturally occuring drift waves which were
observed in some range of plasma parameters. These naturally
occuring drift waves typically have lower azimuthal mode
number (m=3) and longer wavelength (k=5.3 cm^{-1}) with fre-
quencies ranging from 10 - 20 kHz. These drift waves were
observed in plasmas with all concentration ratios, although
the activity was somewhat stronger in a pure helium plasma.
The measured dispersion relation of these drift waves were
found to obey the same drift wave dispersion relation shown
by Eq. (17). However, we did not observe any parametric
coupling of such waves with the pump RF electric field.
This lack of parametric coupling can be explained by a
simple wave number matching condition argument. In our
experiments, we are restricted to an RF oscillator with
$f_0 \geq$ 2MHz and the magnetic field B $\leq$ 4.2 kG which for a
helium plasma yeild the condition, $\omega_0/\Omega_{He} \geq 1.25$. Since

the sideband mode is the electrostatic ion cyclotron wave,
for $|f^-| = f_0 \gtrsim 2$ MHz and $T_e \approx 3$eV, the wavelength is $\lambda \leq 0.7$ cm,
or $k \gtrsim 9.0$ cm^{-1}. From the wave number matching condition,
$|\vec{k}_1| = |\vec{k}_2|$, the above restriction suggests that the para-
metric coupling can take place only with drift waves with
wavelength less than 0.7 cm. For this reason, the naturally
occuring drift waves with typical wavelengths of $\lambda \approx 1.2$ cm
could not parametrically couple to the pump RF electric
field. Instead, the shorter wavelength drift waves ($\lambda \approx 0.6$ cm,
$k = 10.5$ cm^{-1}, $m = 6$, $f \approx 25 \sim 40$ kHz) which can satisfy
the wave number matching condition were excited in our experi-
ments.

VII: SUMMARY AND DISCUSSIONS:

We have experimentally and theoretically investigated parametric instabilities excited by a pump with a frequency near the ion cyclotron frequency in multi-ion-species plasmas. The general dispersion relation of parametric coupling in the frequency range has been derived, including the ion drift motion in multi-ion species plasmas.

In order to test the theory, we have carried out experiments in the Princeton L-4 device. An induction coil was designed and constructed to impress a radially uniform RF electric field of sufficiently large amplitude inside the plasma column. With this induction coil, we observed and investigated two types of parametric instabilities in multi-ion-species plasmas:

(1) Electrostatic Ion Cyclotron Waves (ESICW) - In a two-ion-species plasma the electrostatic ion cyclotron waves are excited above each ion cyclotron frequency (Section IV, Part A).

(2) Drift Wave - In a two-ion-species plasma, in the region with large density gradients, drift waves are excited with the electrostatic ion cyclotron waves at the upper and lower sidebands (Section IV, Part B).

The experimental data were generally found to be in good agreement with the theory. The ESICW and drift wave

excitations are both driven by the relative ion-ion drift motion, and this driving mechanism requires the presence of at least two ion species in the plasma.

In this experiment, the following new measuring techniques were tested and utilized:

1. A combined spectroscopic-Langmuir probe techniques was used to measure the ion concentration ratio.

2. The ion concentration ratio was also obtained from the dependence of the ESICW dispersion relation on the ion concentration ratio.

3. The ion temperature was obtained from the behavior of the ESICW dispersion relation near the second harmonic of the ion cyclotron frequency.

In addition, we have also experimentally verified the dispersion relations of the ESICW and the drift wave in a two-ion-species plasma. Strong resonance behavior of the ESICW near the ion-ion hybrid frequency was observed.

If one is to apply the result of the present work to the I RF experiments in fusion devices, one has to first consider the effect of the finite ion temperature (i.e., $T_e \simeq T_i$). For $T_e \simeq T_i$, the theory predicts a significantly higher threshold electric field, typically $U/C_s = O(1)$, for the ESICWs excitation[7], and thus, this decay process may not be of importance in the ICRF experiments. For drift wave excitation, the extrapolation to tokamak plasmas is

difficult due to the fact that the drift wave properties in a toroidal device, such as a tokamak, are considerably different from our linear device.[43] However, we have shown that in a two-ion-species plasma the RF does provide a destabilizing term in the parametric coupling equation and if the condition permits, it can enhance the existing drift wave activities, or can destabilize new ones. We also note that aside from the enhancement of drift wave activities, this decay process would deposit most of the energy into the sidebands (the electrostatic ion cyclotron waves) which can heat electrons via electron Landau damping or ions via ion cyclotron damping. The present phenomena can be investigated in ICRF heating experiments by corre-lating the drift wave activities which can be measured by microwave[44] or laser scattering techniques[45] with the plasma parameters. Clearly more experimental and theoretical work needs to be done to access the true consequence of the present parametric processes on future ICRF experiments.

ACKNOWLEDGMENTS

APPENDIX A

With $\omega = x + iy$, Eq.(13) can be written in the following form:

$$(x-\omega_1) + i(\Gamma_2 + y) = K\omega_1\omega_2 \left[\frac{1}{(x+\delta) + i(\Gamma_2+y)} - \frac{1}{(x-\delta) + i(\Gamma_2+y)} \right],$$

where K is defined as, $\qquad\qquad$ (A-1)

$$K = \frac{(\omega_1-\omega_2)^2 \cdot [Re(\chi_1-\chi_1^0)]^2}{4 \; \partial\epsilon/\partial\omega_1 \; \partial\epsilon/\partial\omega_2 \; \omega_1 \; \omega_2} \qquad .$$

By separating Eq. (A-1) into real and imaginary parts, we obtain the following two independent equations:

$$x-\omega_1 = F(x,y) \; [\delta^2-x^2+(\Gamma_2+y)^2] \quad , \qquad\qquad (A-2)$$

and

$$\Gamma_1 + y = F(x,y) \quad 2 \; x \; (\Gamma_2+y) \qquad , \qquad\qquad (A-3)$$

where

$$F(x,y) = \frac{2K \; \omega_1\omega_2 \; \delta}{[(x+\delta)^2 + (\Gamma_2+y)^2] \; [(x-\delta)^2 + (\Gamma_2+y)^2]} \quad . \qquad (A-4)$$

Using Eq. (A-2) and (A-3) and eliminating $F(x,y)$, one can obtain a quadratic equation in x;

$$D_1 x^2 \quad - \omega_1 x - C_1 = 0 \qquad\qquad\qquad (A-5)$$

where

$$D_1 = 1+(1/2)(\Gamma_1+y)/(\Gamma_2+y)$$

and

$$C_1 = (1/2)(\Gamma_1+y)(\Gamma_2+y) + (1/2)\delta^2(\Gamma_1+y)/(\Gamma_2+y) \quad .$$

Now, it is straight forward to solve for x. Since there are two solutions for x, we choose the root, $x \to \omega_1$ in the limit of small Γ_1, Γ_2 and y. Then x is written as,

$$x = \frac{\omega_1}{2D_1} + \left[\left(\frac{\omega_1}{2D_1} \right)^2 + \frac{C_1}{D_1} \right]^{1/2} \quad . \tag{A-6}$$

One can substitute the expression for x in Eq. (A-3) and obtain the following solution for K (which is proportional to the pump power):

$$K = \frac{(\Gamma_1 + y)}{4\omega_1\omega_2\delta(\Gamma_2+y)} \left\{ \omega_1'^3 + 2\omega_1' [\alpha^2 - \delta^2 + (\Gamma_2+y)^2] \right.$$
$$\left. + \frac{\omega_1'^2\alpha^2 + [\alpha^2+\delta^2 + (\Gamma_2+y)^2]^2 - 4\delta^2\alpha^2}{[\omega_1'/2 + (\omega_1'^2/4 + \alpha^2)^{1/2}]} \right\} \quad . \tag{A-7}$$

where $\omega_1' = \omega_1/D_1$ and $\alpha^2 = C_1/D_1$. From Eq. (A-7), it is now straight forward to calculate the necessary pump power K to destabilize the instability with a growth rate y.

The threshold condition can be obtained from Eq. (A-7) by letting $y = 0$ which yields the threshold pump power. Similarly, from Eq (A-6) one can obtain the excited frequency of the low frequency mode at the threshold pump power.

APPENDIX B: $|\phi^-|/|\phi^+|$

In deriving expression for ϕ^-/ϕ^+, we shall use the
same approximations and notations as used in Section II.
Using Eq.(3) and keeping terms up to $O(\mu_\sigma^2)$ and eliminating
ϕ, one obtains an expression for ϕ^-/ϕ^+ in the following
form:

$$\frac{\phi^-}{\phi^+} = - \frac{\epsilon^+ + \sum_\sigma \left|\frac{\mu_\sigma}{4}\right|^2 (\chi_\sigma - 2\chi_\sigma^+) + Q \left[\sum_\sigma \frac{\mu_\sigma^2}{8} (\chi_\sigma^+ + \chi_\sigma^- - 2\chi_\sigma)\right]}{\epsilon^- + \sum_\sigma \left|\frac{\mu_\sigma}{4}\right|^2 (\chi_\sigma - 2\chi_\sigma) + \frac{1}{Q} \left[\sum_\sigma \frac{\mu_\sigma^2}{8} (\chi_\sigma^+ + \chi_\sigma^- - 2\chi_\sigma)\right]} \quad \frac{1}{Q}$$

(B-1)

where

$$Q = \sum_\sigma \frac{\mu_\sigma^*}{2} (\chi_\sigma - \chi_\sigma^+) / \sum_\sigma \frac{\mu_\sigma}{2} (\chi_\sigma - \chi_\sigma^-) \ .$$

Here Q is a dimensionless quantity which is approximately
unity for all the decay processes which we discuss
in this appendix.   Equation (B-1) can be further
simplified by utilizing the dispersion relation of the
parametric coupling for each decay instability. Since
each of the decay instabilities has a different dispersion
relation, it is necessary to consider each case spearately.

We shall now specialize our analysis to those decays
which were discussed in Section II.

1. Electrostatic Ion Cyclotron Wave Excitation:

This decay was briefly discussed in Section II and will
be presented in more detail in Section IV. For this decay
ϵ and ϵ^- are small (i.e. ϵ, $\epsilon^- << \chi_\sigma, \chi_\sigma^-, \epsilon^+$) and $\epsilon\epsilon^- = O(\mu_\sigma^2 \chi_\sigma^2)$.
then most of the terms of $O(\mu_\sigma^2)$ in Eq. (B-1) can be neglected
and then Eq.(B-2) takes on the following simple form:

$$\frac{\phi^-}{\phi^+} = -\frac{\varepsilon^+}{\varepsilon^-} \quad Q = -\frac{\varepsilon^+}{\varepsilon^-} \frac{\sum\limits_i \frac{\overset{\star}{\mu_i}}{2}(\chi_i - \chi_i^+)}{\sum\limits_i \frac{\mu_i}{2}(\chi_i - \chi_i^-)} \quad . \tag{B-2}$$

Here we have used the relation, $\chi_e = \chi_e^+ = \chi_e^-$. The relative amplitude of the sidebands fluctuation which we obtained from the spectrum analyzer in our experiments is actually an absolute value of ϕ^-/ϕ^+. Therefore by taking the absolute value of Eq.(B-2), one obtains the following relation:

$$|\phi^-| /|\phi^+| = (|\varepsilon^+|/|\varepsilon^-|) A \quad . \tag{B-3}$$

where A is a variable of O(1). The exact value of A depends on the parametric excitation which has to be calculated using the experimental parameters. We note that $|\phi^-|/|\phi^+|$ is independent of the pump electric field strength as long as γ, the growth rate of the decay, is small compared to $|\varepsilon^-|$.

2. Drift Wave Excitation:

The theory for this decay was discussed in Section II and also in Appendix A. For this decay, ε and ε^+ are small (i.e. ε, $\varepsilon^+ << \chi_\sigma$, χ_σ^+) and $\varepsilon \, \varepsilon^+ = O(\mu_\sigma^2 \chi_\sigma^2, \mu_\sigma^2 (\chi^+)^2)$. Then most of the terms in Eq.(B-1) which are of $O(\mu_\sigma^2)$ can be neglected and one obtains the same relation as expressed

by Eq. (B-2). One can further simplify Eq. (B-2) for this decay by noting $\chi_e \simeq \chi_e^- \simeq \chi_e^+$ and $\chi_i^+ \simeq \chi_i^- \simeq \chi_i^0$. Then Eq. (B-2) takes on the following simple form:

$$\phi^-/\phi^+ = -(\epsilon^+/\epsilon^-) \ (\mu_1^* - \mu_2^*)/(\mu_1 - \mu_2). \tag{B-4}$$

Using the same notation used in Section II, one can further simplify Eq. (B-4) to the following form:

$$\frac{\phi^-}{\phi^+} = \frac{(i\Gamma_2 + \omega + \delta)}{(i\Gamma_2 + \omega - \delta)} \ \frac{(\mu_1^* - \mu_2^*)}{(\mu_1 - \mu_2)} \tag{B-5}$$

where Γ_2 is the linear damping rate of the sideband, ω is the drift wave frequency, and δ is the frequency mismatch term. The absolute value of Eq. (B-5) takes on the following simple form:

$$\frac{|\phi^-|}{|\phi^+|} = \frac{\Gamma_2^2 + (\omega + \delta)^2}{\Gamma_2^2 + (\omega - \delta)^2} \ . \tag{B-6}$$

The values of δ, Γ_2 and ω depend on the experimental parameters. We note that $|\phi^-|/|\phi^+| \to 1$ as $\Gamma_2/\omega \approx \delta/\omega \to \infty$, and for our experiment, typically $|\phi^-|/|\phi^+| \simeq 1.1$.

APPENDIX C: NEUTRAL LINE INTENSITY VS ION DENSITY

The helium neutral line 5015Å emission takes place
when the 3P state of HeI atom radiates down to the 2S
state.[28]   HeI is a state of a neutral helium in which one
of the two bounded electrons is in the ground state and
the other is in the excited state.   This is a usual state
of excited helium neutral atom in a relatively low temp-
erature (few eV), weakly ionized plasma (in our plasma
the ionization is less than 0.1%).   Furthermore, this
electric-dipole radiative process takes only a few nano-
seconds so that it is not subjected to the electron
collisions which can scatter the 3P state into the neigh-
boring states.   This is true for a plasma with $n_o \leq 10^{12} \text{cm}^{-3}$.
For this reason, the 5015Å emission intensity is a good
indicator for the 3P state excitation in our plasma.

The 3P state excitation rate is in turn related to
the ionization rate since the 3P state energy level is
close to the ionization energy ($\varepsilon \approx 25\text{eV}$) so that it
takes almost as much energy to induce the 3P state
excitation as to cause the ionization.   Due to the impor-
tance and simplicity of the helium atom, this type of
interaction has been studied in detail in spectroscopy and
atomic physics.   In Ref 29, a summary of the past researches
on the 5015Å line excitation can be found.   In a similar
review article,[30] the ionization process for the neutral

atom is considered. From such work, one can obtain a
good linear relation of the 5015Å line to the ionization
rate. It is important to note that the proportionality
factor which relates these two quantities is relatively
insensitive to the energy distribution of the energetic
electrons ($\varepsilon \geq 25eV$).[31] This is quite convenient since
the energy distributions of the energetic electrons are
only approximately known in our plasma.

One can relate the ionization rate to the ion density
by noting that in a steady-state plasma, the ion density
is proportional to the ionization rate. The proportionality
factor, the density decay time, is expected to stay reasonably
constant in our open ended linear device (no mirror field).
One can actually measure this proportionality factor by measuring
the 5015Å line intensity as a function of the ion saturation
current. As shown by Fig.3(a), we find experimentally
that the 5015Å intensity is linearly related to the ion
saturation current for a wide range of the plasma parameters.

The neon line (5852Å) is less well known. This line
is emitted when 3P state of NeI atom radiates down to the
3S state.[28] This line emission is related to the 3P state
excitation rate. Just as for the helium line, the energy
level of the 3P state is reasonably close to the ionization
energy level. Therefore, the impact excitation rate of the
3P state and the ionization rate is related to each other.
Experimentally we find that the neon line intensity is

linearly related to the neon ion density as shown by Fig 3(a).
The non-linearlity at the high density region in Fig. 3(a)
may be due to collisional effects since this process
takes a longer time compared to that of the helium line.

Finally, we note that in all the processes discussed here,
the ionization and the neutral line emission can be induced
only by the energetic electrons produced by the plasma source.
The bulk electrons with $T_e \approx 2-4$ eV do not contribute since
the required energy for the processes to occur is relatively
large ($\varepsilon \gtrsim 20$ eV).

APPENDIX D: COLLISIONAL EFFECTS ON THE WAVES

We calculate the ion susceptability using the fluid equation with the Krook-type collision operator [46] to model the momentum transfer by the collisions. Since in our experiment, $k\rho_i \ll 1$ is usually satisfied, one can neglect the ion viscous damping effect. Then the Krook-type collisional model is quite adequate to describe the ion-neutral collisions and the ion-ion collisions among the ions of different species since these processes can be characterized by simple momentum transfers. With the above assumptions the fluid momentum equations for the each of the ion species can be written in the following form:

$$- i\omega_i \, m_i \, N_i \, \vec{V}_i = -iN_i \, \vec{k}e\phi + N_i m_i \, \vec{V}_i \times \vec{\Omega}_i + \nu_{ji} N_j m_j \vec{V}_j \qquad \text{(D-1)}$$

and

$$\omega_i = \omega + i\nu_{io} + i\nu_{ij} \quad ,$$

where

ν_{io} is the ion-neutral collision frequency, ν_{ij} is the ion-ion collision frequency for the ions of the species i to collide with the ions of species j, and N_j is the relative ion concentration.

The continuity equation for the ion species i can be written in the following form:

$$\frac{dn_i}{dt} = - i\omega n_i + N_i n_0 \vec{\nabla} \cdot \vec{V}_i + V_{ix} N_i \frac{\partial \, n_0}{\partial \, x} \qquad \text{(D-2)}$$

Here we assumed a plasma density gradient, $\partial n_0/\partial x$, in the $\hat{x}$ - direction. n_i and $\vec{V}_i$ are the perturbed density and velocity.

One can solve Eqs. (D-1) and (D-2) for n_i by eliminating V_i and expanding in powers of (ν/ω), which is a small quantity. After some algebra, one obtains an expression for n_i to the first order in (ν/ω) in the following form:

$$\frac{n_i}{n_o} = \frac{N_i}{m_i} \ \frac{e\phi}{D_i} \ \frac{\omega_i}{\omega} \ \left[k_\perp^2 + \frac{\partial n_o}{\partial x} \ (-ik_x + \frac{\Omega_i}{\omega_i} k_y) \right]$$

$$+ \ i \ \frac{\nu_{ji}}{\omega} \ \frac{N_j \, e\phi}{m_i D_i D_j} \ \left[A \ (k_\perp^2 - i\frac{\partial n_o}{\partial x} k_x) + \omega(\Omega_i + \Omega_j) k_y \right]$$

where $\hspace{10em}$ (D-3)
$$D_i = \omega_i^2 - \Omega_i^2 \quad \text{and} \quad A = \omega^2 + \Omega_i \Omega_j .$$

Using Eq. (D-3) we considered two types of waves which are important in our experiment.

1. The electrostatic ion cyclotron wave: Since the frequency of the mode is near the ion cyclotron frequency, one can assume that the gradient term is small. This is equivalent to assuming that the drift frequency is small compared with the ion cyclotron wave frequency. Then Eq. (D-3) simplifies to the following form:

$$\frac{n_i}{n_0} = \frac{N_i}{m_i} \ \frac{e\phi \ k^2}{(\omega^2 - \Omega_i^2)} \ - \ i \ \frac{(\nu_{i0} + \nu_{ij})}{\omega} \ \frac{(\omega^2 + \Omega_i^2)}{(\omega^2 - \Omega_i^2)} \ \frac{N_i}{m_i} \ \frac{e\phi \ k^2}{(\omega^2 - \Omega_i^2)}$$

$$+ \ i \ \frac{\nu_{ji}}{\omega} \ \frac{(\omega^2 + \Omega_i \Omega_j)}{(\omega^2 - \Omega_j^2)} \ \frac{N_j}{m_i} \ \frac{e\phi \ k^2}{(\omega^2 - \Omega_i^2)} \hspace{4em} \text{(D-4)}$$

2. The drift wave: The drift wave usually occurs for the frequency $\omega \ll \Omega_i$ and it is appropriate to expand in (ω/Ω_i) as well. Then to the leading order in $O(\omega^2/\Omega_i^2)$ Eq. (D-3) can be written in the following form:

$$\frac{n_i}{n_o} = -\frac{N_i}{m_i} \frac{e\phi}{\Omega_i^2} \left[k_\perp^2 \left(1 + \frac{i\nu_{io}}{\omega} + \frac{i\nu_{ij}}{\omega} \right) + \frac{\partial n_o}{\partial x} k_y \frac{\Omega_i}{\omega} \right]$$

$$+ i \frac{N_j}{m_i} \frac{e\phi}{\Omega_i \Omega_j} \frac{\nu_{ji}}{\omega} k_\perp^2 . \tag{D-5}$$

One can see from Eq.(D-5), the ion-ion collision terms vanish when summed over the both ion species which is resonable for the low frequency wave where both ion species oscillate in the same phase.

REFERENCES

[1] J. Adam, M. Chance, H. Eubank, W. Getty, E. Hinnov, W. Hooke, J. Hosea, F. Jobes, F. Perkins, R. Sinclair, J. Sperling, and H. Takahashi, in Proceeding of the Fifth Conference on Plasma Physics and Controlled Nuclear Fusion Research, Tokyo, Japan, 1974, Vol II, P. 65.

[2] H. Takahashi, C.C. Daughney, R.A. Ellis, R.J. Goldston, H. Hsuan, T. Nagashima, F.J. Paoloni, A.J. Sivo, and S. Suckewer, Phys. Rev. Lett. 39, 31 (1977).

[3] A.A. Ivanov and V.V. Parail, JETP 35, 494 (1972).

[4] K.D. Harms, G. Hasselberg, and A. Rogister, Nuclear Fusion 14, 251 (1974).

[5] A.B. Kitsenko and K.N. Stepanov, JETP 37, 813 (1973).

[6] K.D. Harms, G. Hasselberg, and A. Rogister, Nuclear Fusion 14, 657 (1974).

[7] J.L. Sperling and F.W. Perkins, Phys. Fluids 17, 1857 (1974)

[8] Y. Satya, A. Sen, and P. Kaw, Nuclear Fusion 15, 195 (1975).

[9] M. Ono, R.P.H. Chang, and M. Porkolab, Phys. Rev. Lett. 38, 962 (1977).

[10] M. Ono, Ph.D. Thesis, Princeton University, (1978).

[11] M. Ono, P. Porkolab, and R.P.H. Chang, Phys. Lett. A 67, 379 (1978).

[12] S. Yoshikawa, M.A. Routhman, and R.M. Sinclair, Phys. Rev. Lett. $\underline{14}$, 214 (1965).

[13] J.M. Dawson, H.C. Kim, D. Arnush, B.D. Fried, R.W. Gould, L.O. Heflinger, C.F. Kernel, T.E. Romesser, R.L. Stenzel, A.Y. Wong, R.F. Wuerker, Phys. Rev. Lett. $\underline{37}$, 1574 (1976).

[14] Y.M. Aliev, V.P. Silin, and C. Watson, JETP $\underline{23}$, 626, (1966).

[15] T. Amano and M. Okamoto, J. Phys. Soc. Japan $\underline{24}$, 916 (1968).

[16] M. Porkolab, Phys. Fluids $\underline{20}$, 2058 (1977).

[17] T.H. Stix, Theory of Plasma Waves (McGraw-Hill, New York, 1962), P226.

[18] S.J. Buchsbaum, Phys. Fluids $\underline{3}$, 418 (1960).

[19] M. Porkolab and R.P.H. Chang, Phys. Fluids $\underline{13}$, 2054 (1970).

[20] D. Pesme, G. Laval, and R. Pellat, Phys. Rev Lett. $\underline{31}$, 203 (1973).

[21] K. Nishikawa, J. Phys. Soc. Japan $\underline{24}$, 916 (1968).

[22] N.A. Krall and A.W. Trivelpiece, Principles of Plasma Physics (McGraw-Hill, New York, 1973), P. 206.

[23] M. Porkolab, Phys. Fluids $\underline{11}$, 834 (1968).

[24] R. Limpacher and K.R. Mackenzie, Rev. Sci. Instrument $\underline{44}$, 726 (1973).

[25] S. Bernabei, Private Communication.

[26] J.G. Laframboise, Univ. of Tronto, Inst. for Aerospace Studies, Report 100 (1966).

[27] P.K. Fisher and R.W. Gould, Phys. Fluids $\underline{14}$, 857 (1971).

[28] W.L. Wiese, M.W. Smith, and B.M. Glennon, Atomic Transition Probabilities, NSRDS-NBS4, Vol I.

[29] B.L. Moiseiwitsch and S.J. Smith, Rev. Mod. Phys. $\underline{40}$, 238 (1968).

[30] L.J. Kieffer and G.H. Dunn, Rev. Mod. Phys. $\underline{38}$, 1 (1966).

[31] E. Hinnov, Private Communications.

[32] S.C. Brown, Basic Data of Plasma Physics. The Technology Press and John Wiley and Sons, Inc., N.Y. (1959).

[33] J.B. Hasted and R.A. Smith, Proc. Roy. Soc. A205, 421 (1951).

[34] J.D. Jackson, Classical Electrodynamics (John Wiley & Sons, New York, 1962), P. 141.

[35] J.P.M. Schmitt, Phys. Rev. Lett. $\underline{31}$, 982 (1973).

[36] A. Hirose, I. Alexeff, and W.D. Jones, Phys. Fluids $\underline{13}$, 2039 (1970).

[37] E.R. Ault and H. Ikezi, Phys. Fluids $\underline{13}$, 2874 (1970).

[38] T. Ohnuma, S. Miyake, T. Sato, and T. Watari, Phys. Rev. Lett. $\underline{26}$, 541 (1971).

[39] Y. Nakamura, M. Nakamura, and T. Itoh, Phys. Rev. Lett. $\underline{37}$, 209 (1976).

[40]M. Ono, Phys. Rev. Lett. 42, 1267 (1979).

[41]R.W. Motley, Q. Machines (Academic Press, New York, 1975).

[42]T.K. Chu, H.W. Hendel, and P.A. Politzer, Phys. Fluids. 11, 2426 (1968). (This also gives references to ealier works.)

[43]W.M. Tang., Nuclear Fusion 18, 1089 (1978).

[44]E. Mazzucato, Phys. Rev. Lett. 36, 792 (1976).

[45]C.M. Surko and R.E. Slusher, Phys. Rev. Lett. 37, 1747 (1976).

[46]Bhatnagar, E.P. Gross, and M. Krook, Phys. Rev. 94, 511, (1954).

FIGURE CAPTIONS

Fig. 1. Theoretical dispersion relation of electro-
static ion cyclotron waves in a helium-neon plasma with
a concentration ratio of He:Ne = 4:6. The typical decay
patterns are indicated by the points where each symbol
(circles, triangles, or squares) represents one particular
decay triplet. The pump with $k_0 = 0$ is represented by
the points on y-axis, and the decay waves are represented
by the points on the dispersion curve.

Fig. 2. Schematic of the experimental set-up.

Fig. 3(a). Calibration curves for the helium and (5015Å)
neon (5852Å) neutral lines, with the helium and neon ion
saturation currents obtained from Langmuire probe measure-
ments. 3(b). Calibration curves of the electron saturation
current versus the ion saturation current in helium and neon
plasmas.

Fig. 4(a). Interferometry set-up to measure the
electrostatic ion cyclotron wave linear dispersion re-
lation. 4(b). The electrostatic ion cyclotron wave length
versus He:Ne ion concentration ratio. The magnetic field
and the wave frequency is fixed; B=2.37 kG and f=1.25 MHz.
The dots are the experimentally measured values and the
solid line is the theoretical curve. Typical interfer-
ometry output is shown for three representative values
of the ion concentrations.

Fig. 5(a).   Schematic diagram of the RF electrical
circuit. 5(b). Simplified drawing of RF induction coil
structure with a Faraday shield.

Fig. 6.   Two dimensional profile of the induced RF
electric field E_y numerically calculated for a type of
RF current configuration shown in Fig. 5(b).

Fig. 7(a). Radial electric field profiles generated
by the RF induction coil at the center (Z=0) of the structure.
The dots are the experimentally measured values.   The
dotted line is the corresponding theoretical value.   7(b).
Measured RF electric field in the center of the plasma
column versus the RF current through the induction coil.

Fig. 8.   Linear wave dispersion relations of the
electrostatic ion cyclotron waves in He:Ne plasmas obtained
by linear propagation experiments.   The points are the
experimentally measured values, and the solid curves are
theoretical values with $T_i - 1/40$ eV.   The ion concentration
ratios are as marked.

Fig. 9.   Radial profiles of the plasma density, the
RF electric field, and interferometry outputs on the ob-
served electrostatic ion cyclotron decay waves.

Fig. 10.   Parametric decay spectrum. f_{ci}(He) and
f_{ci}(Ne) are the helium and neon ion cyclotron frequencies.
(B = 2.9 kG, f_0 = 2 MHz, He:Ne = 4.6, C_s is the helium
acoustic speed).   The solid and dashed curves are theore-
tical dispersion relation of the electrostatic ion cyclotron

waves for the same plasma parameters as the experimental values for various ion temperatures, as labeled. The ion-ion hybrid frequency is shown for $\omega_{IH}/\Omega_{He} \approx 0.51$.

Fig. 11(a). Decay wave frequency versus magnetic field for various ion concentration ratios (as marked). Circles and dots are the experimentally observed frequencies, and the solid curves are those obtained from theory. $f_0 = 2$ MHz. 11(b). Threshold pump electric field versus the decay wave number. Circles are the experimentally measured values and the solid curve is obtained from theory.

Fig. 12(a). Radial profiles of the plasma density the decay wave amplitude, the RF electric field, and the electron temperature in the drift wave region. 12(b). Parametric decay spectrum. (10 kHz/Div, 1 kHz band width, $B = 3.7$ kG, $f_0 = 2$ MHz, and He:Ne = 5.5:4.5). 12(c). Observed low frequency decay wave amplitude for $E = 8$ \/cm versus the ion concentration ratio shown by dots. The magnetic fields are as labeled. The dashed curve indicates the parameters where the decay is expected to occur from a simple selection rule analysis.

Fig. 13. Observed frequency of parametrically excited drift waves (shown by the dots) versus the magnetic field strength for various ion concentration ratios (as labeled). The pump electric field is fixed at $E = 8$ V/cm. The threshold electric field contour are shown by solid and dotted

curves for various pump electric fields (as labeled). The shaded region is parametrically stable.

Fig. 14.(a). Parametrically excited drift wave frequency versus ion concentration ratio. The dots are the experimentally measured values and the solid line is obtained from theory. The uncertainty in the plasma parameters used in the theory is represented by the shaded region. 14(b). Threshold electric field (minimized with respect to the magnetic field strength) versus the ion concentration ratio. The circles are the experimentally measured values, and the solid line is obtained from theory.
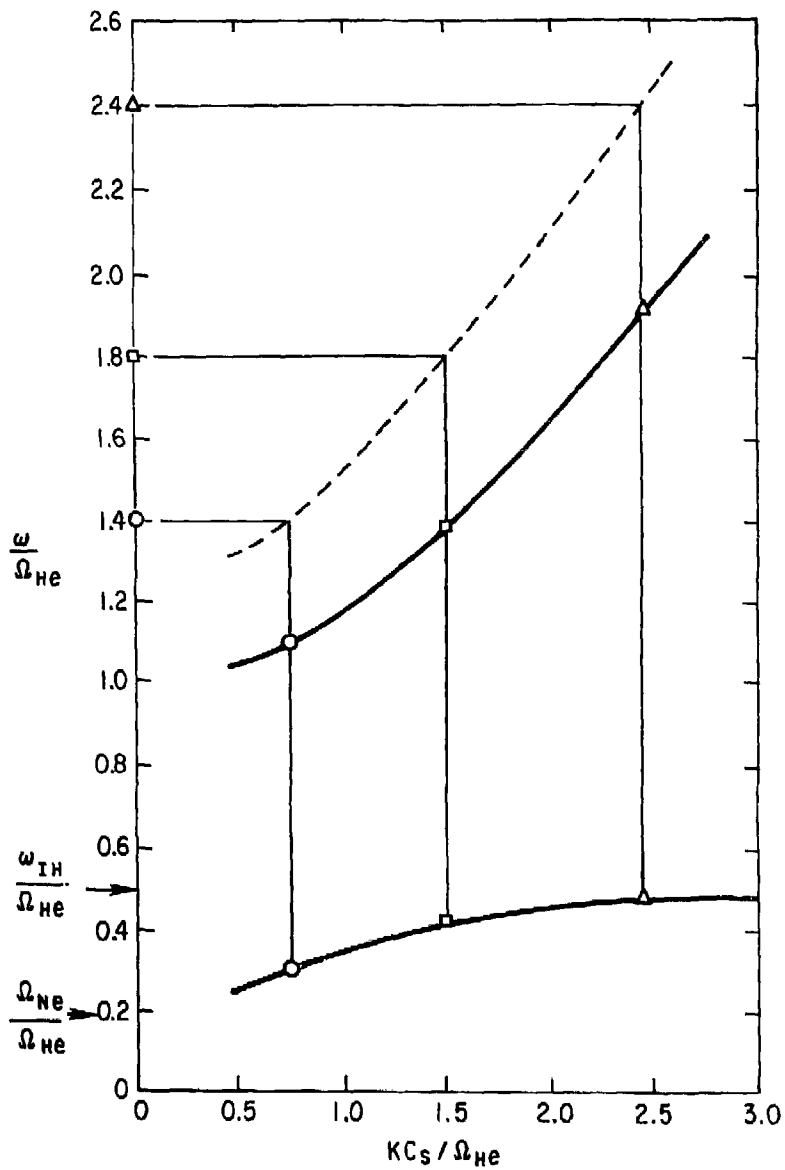
Fig. 1. 783448
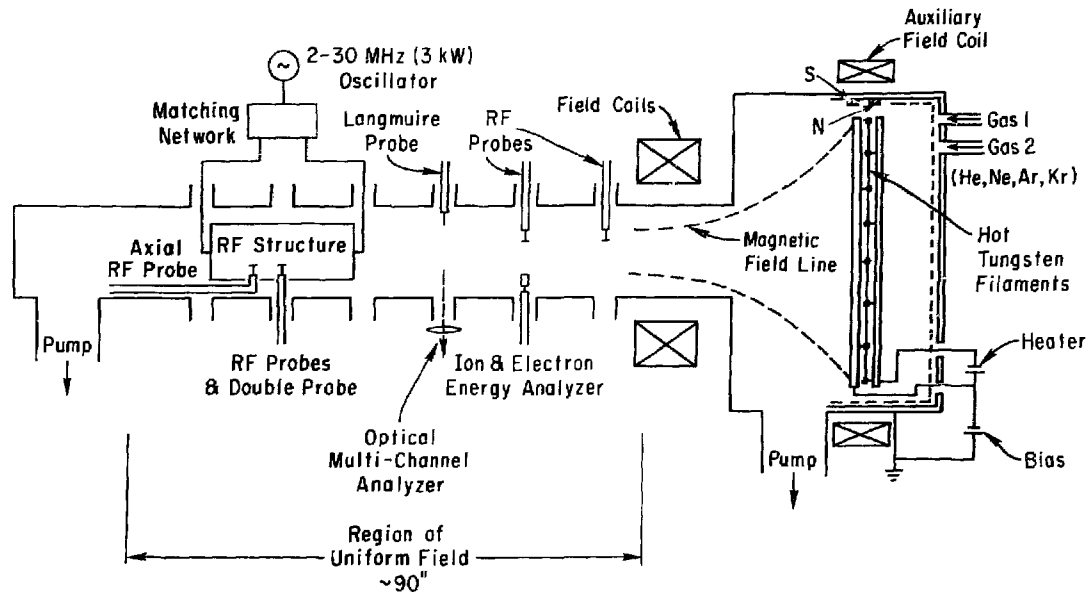
Fig. 2.   793542
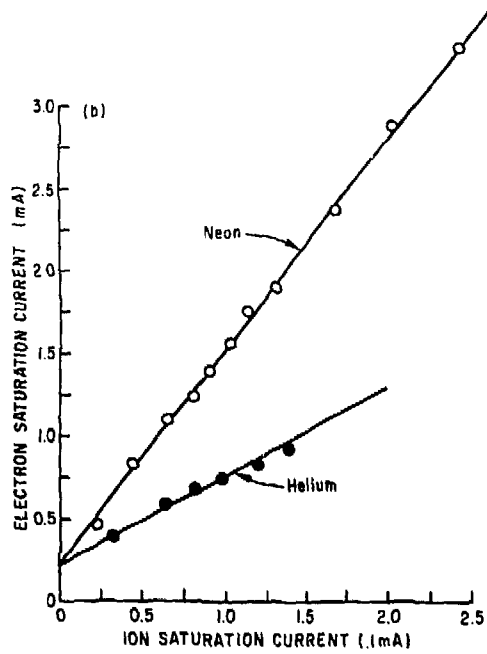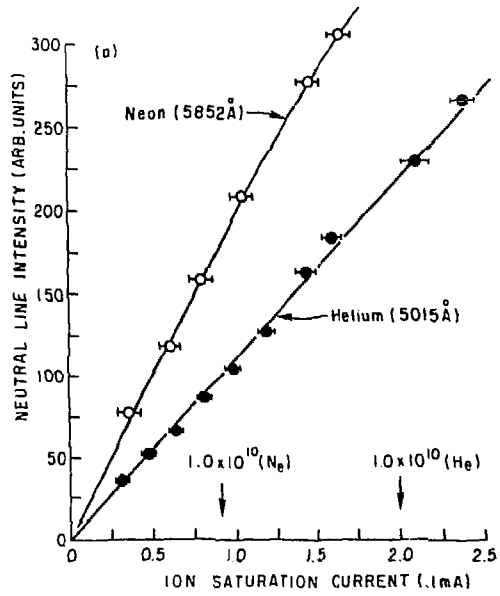
Fig. 3.   793547

(a)
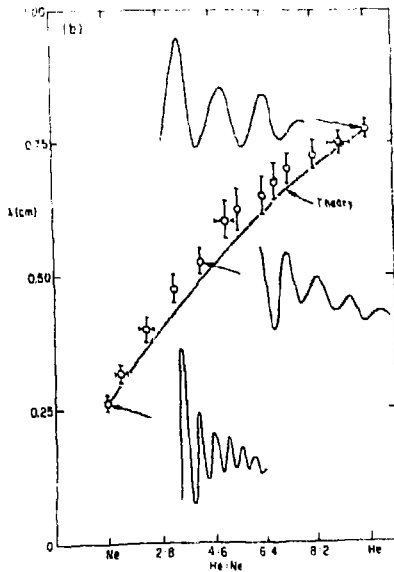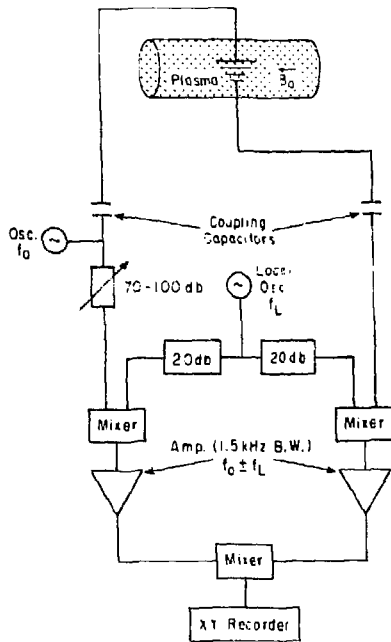
Fig. 4.   793541

(a)

Oscillator (3 kW)

Matching Network

RF Coils

(b)

Radial Probe

B_o

Plasma

Axial Probe

Faraday Shield

Ceramic

Induction Coil

Fig. 5.   793539

-73-
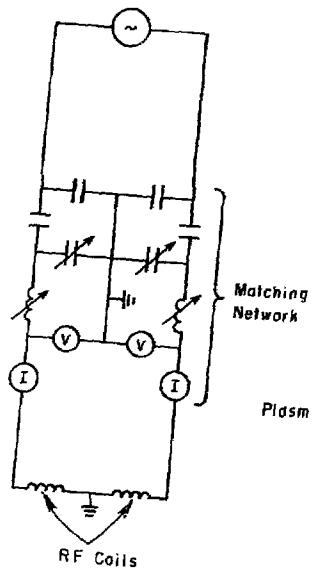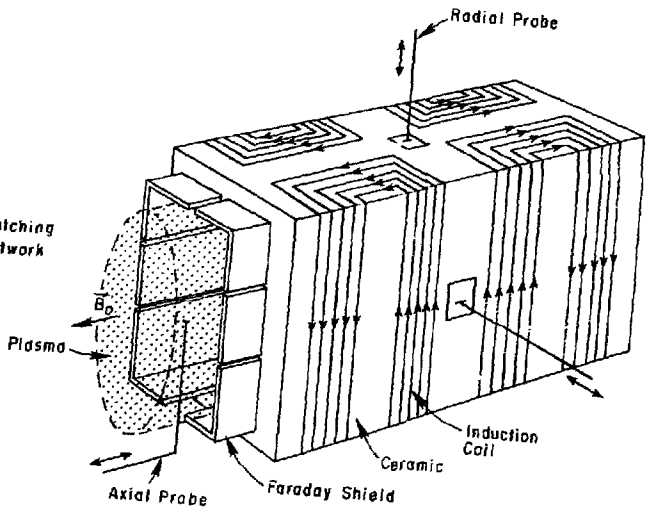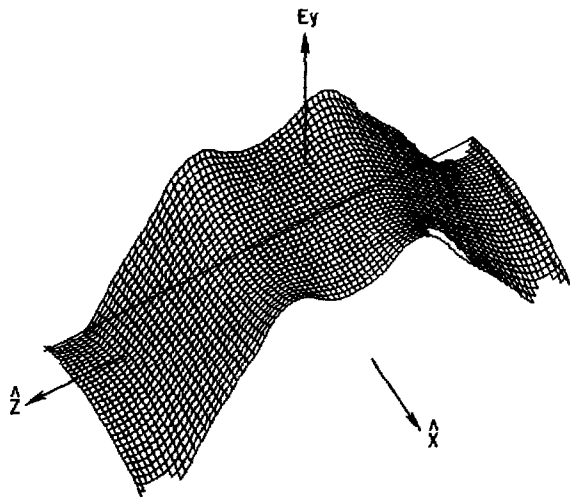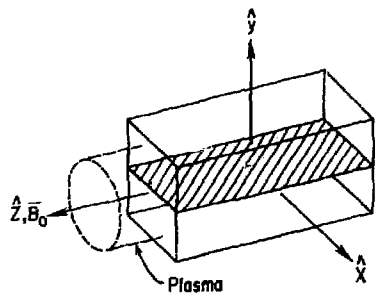
Fig. 6.   762361
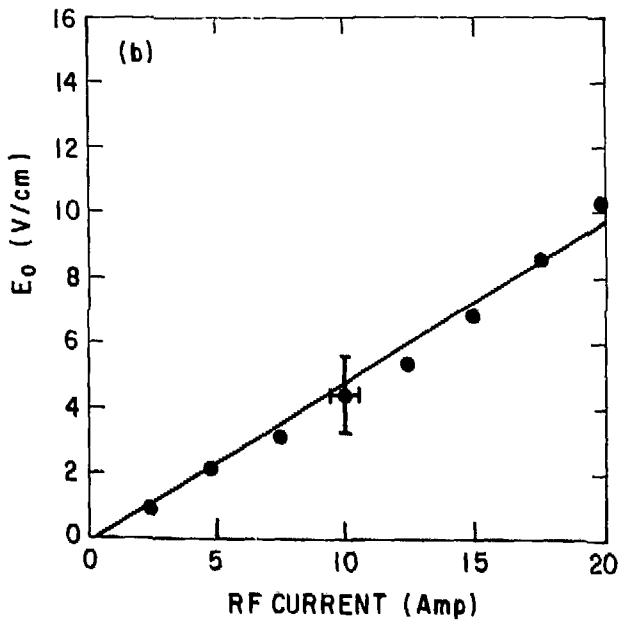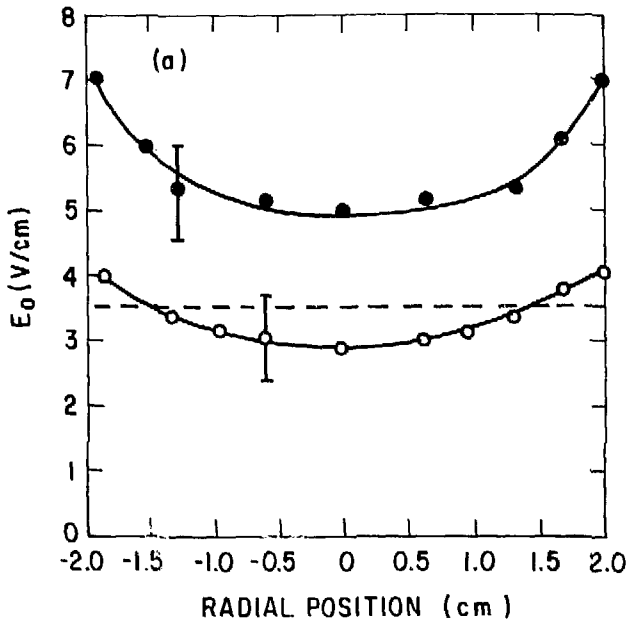
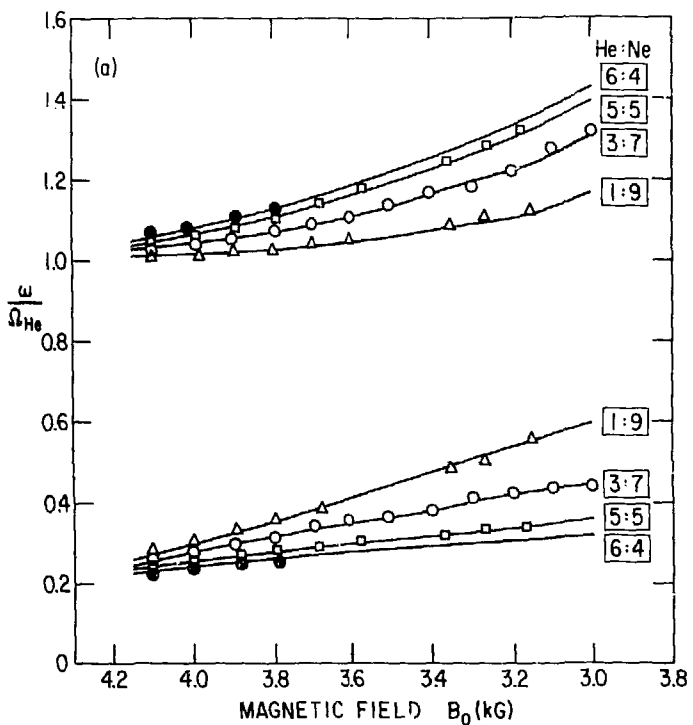Fig. 7.   793548
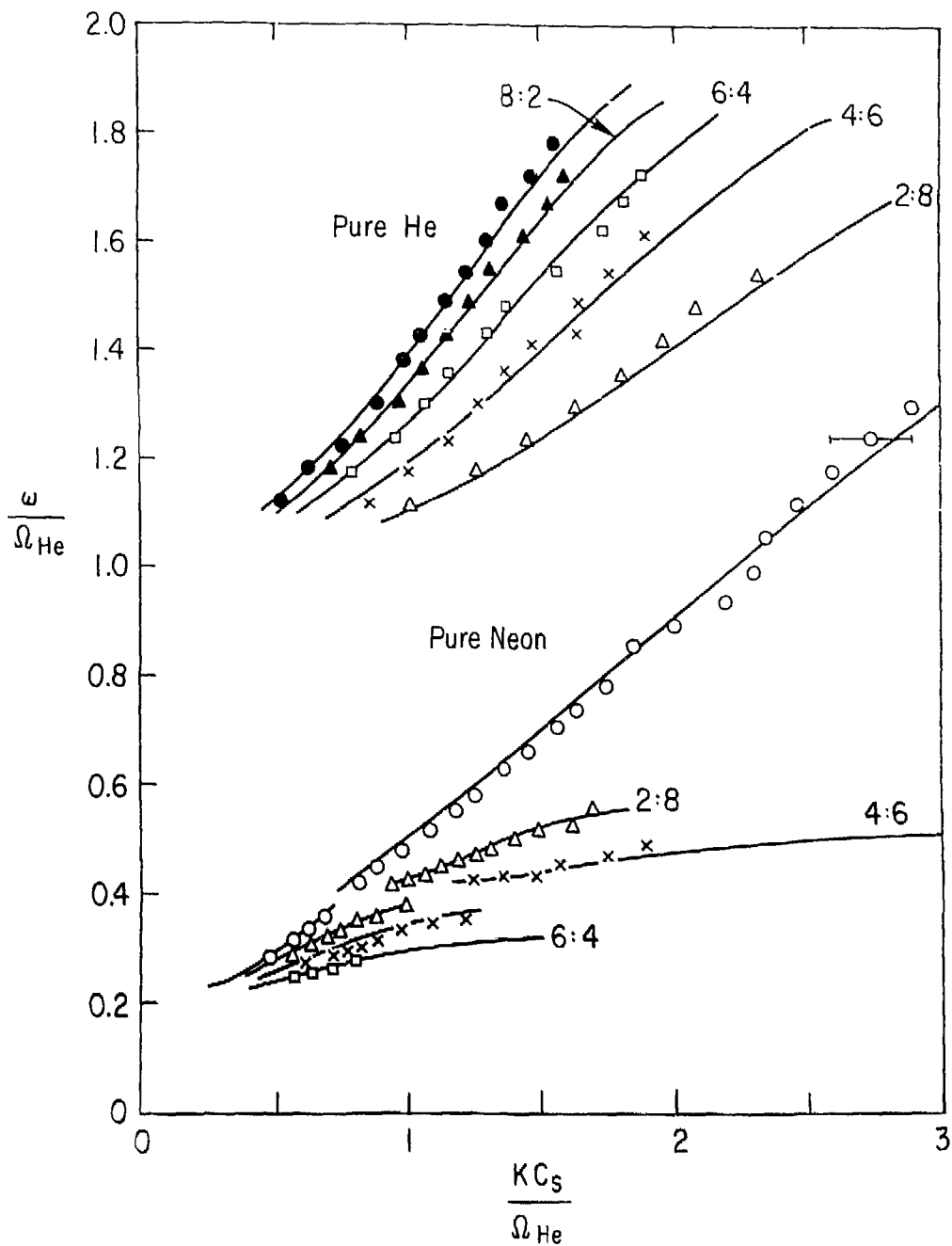
Fig. 8.   793585
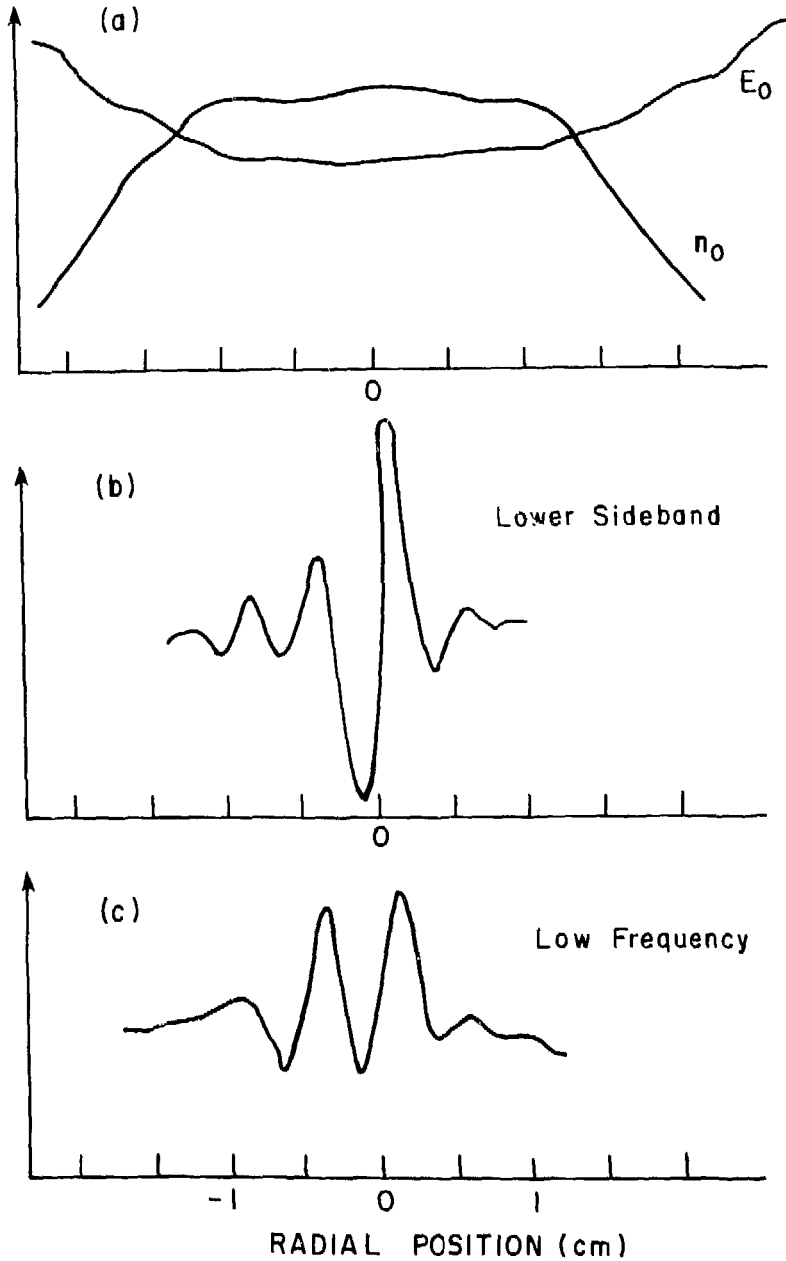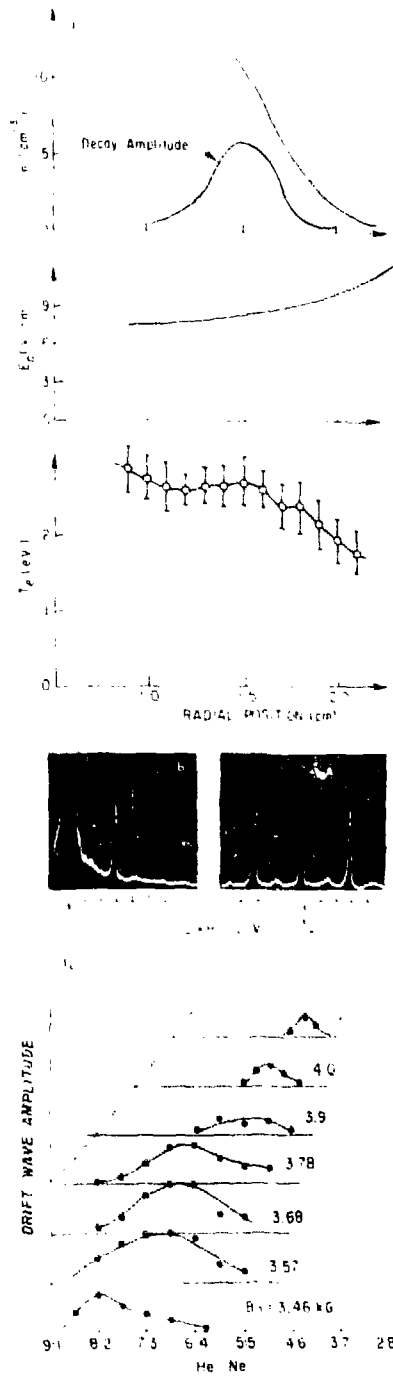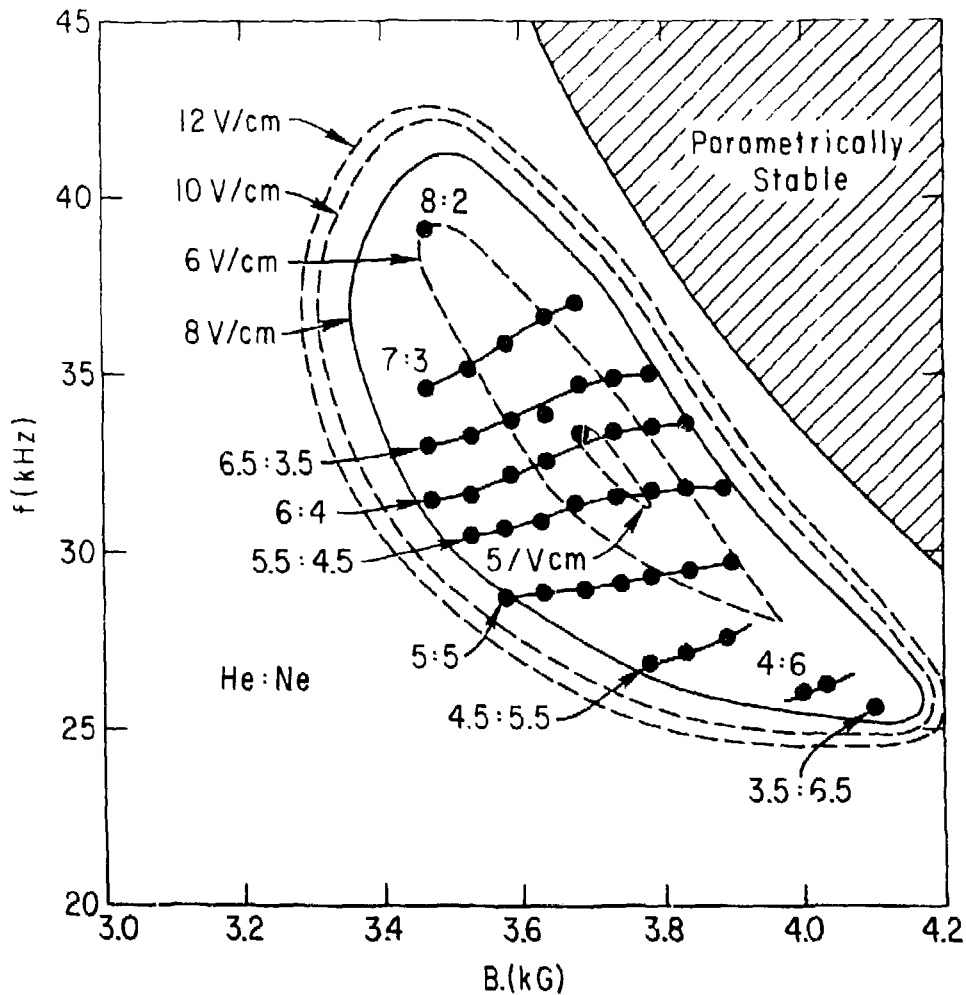
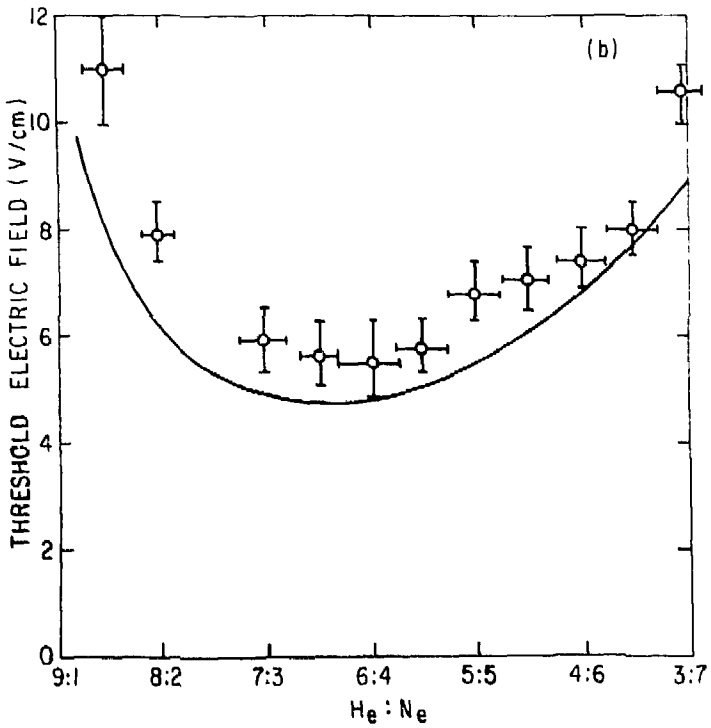Fig. 9.   793550
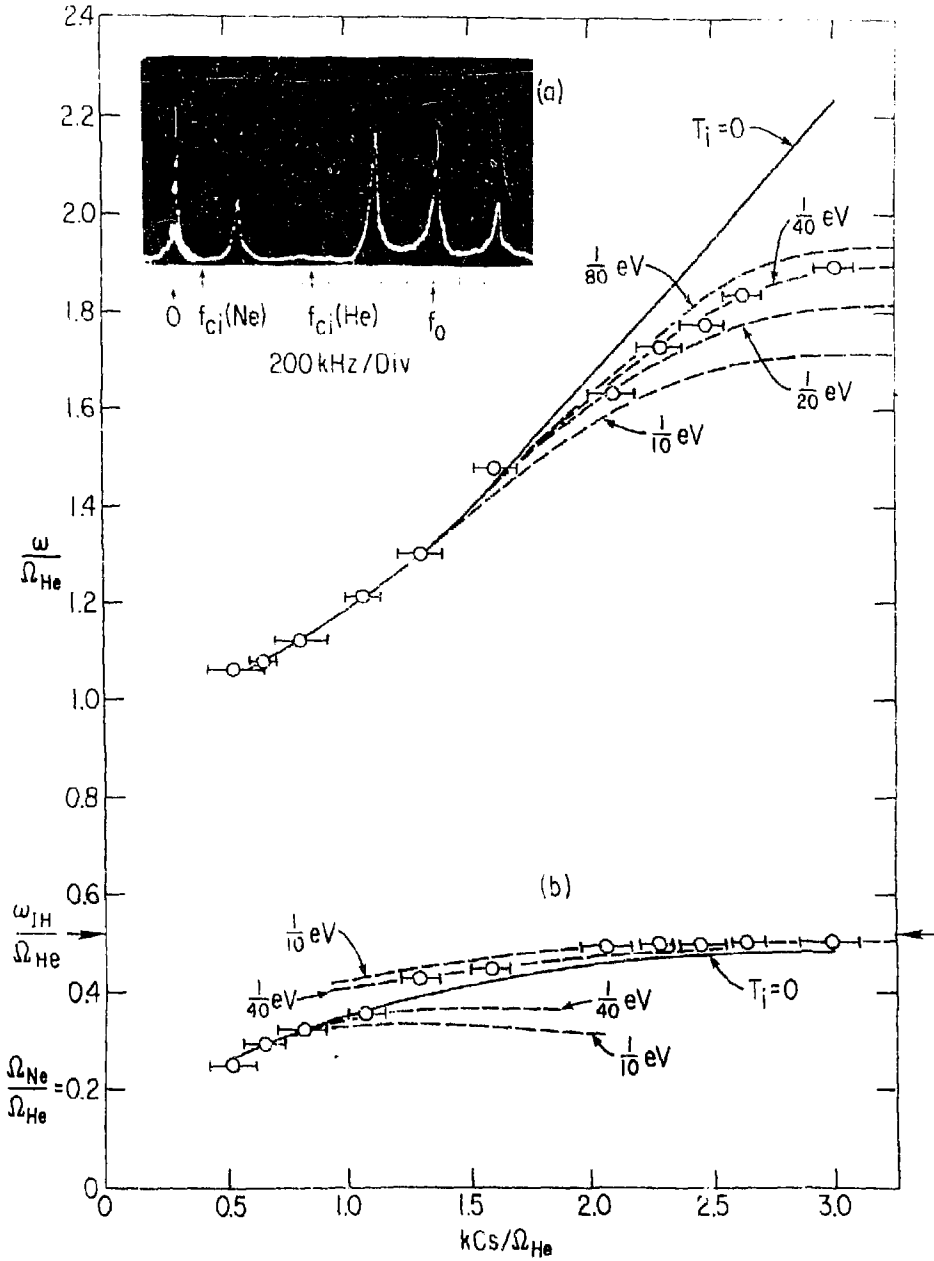
Fig. 10.   783445
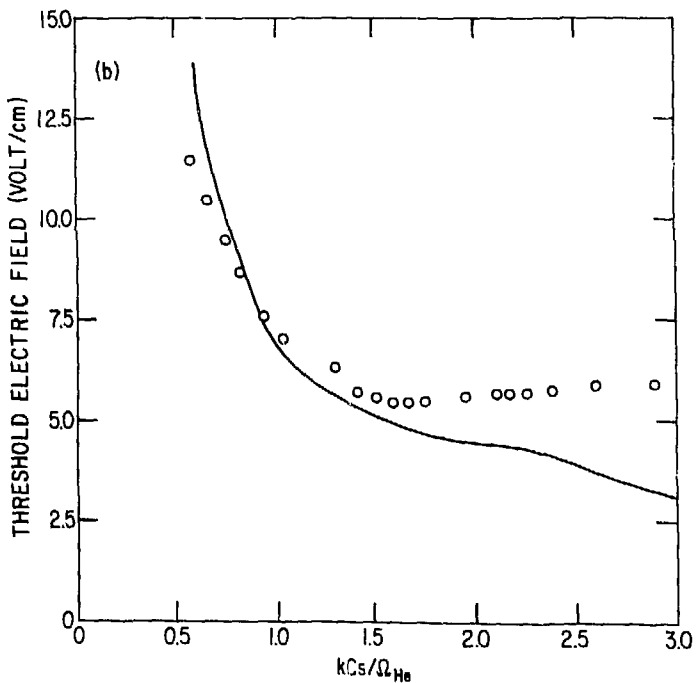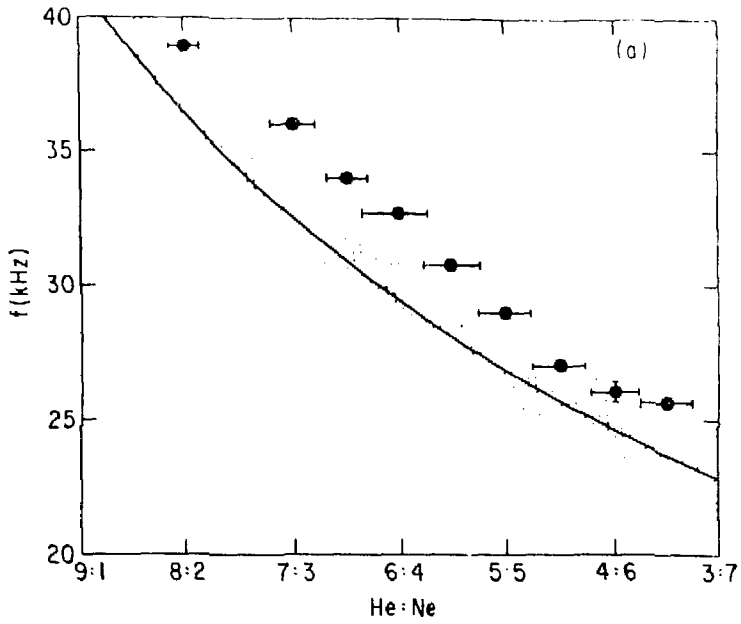
Fig. 11.   772048

Fig. 12. 793537

Fig. 13.   793538

Fig. 14.   793543